Chapter 4

Developing the non-invasive use of micro-Raman spectroscopy for the determination of biomolecular composition in *Chlamydomonas reinhardtii*

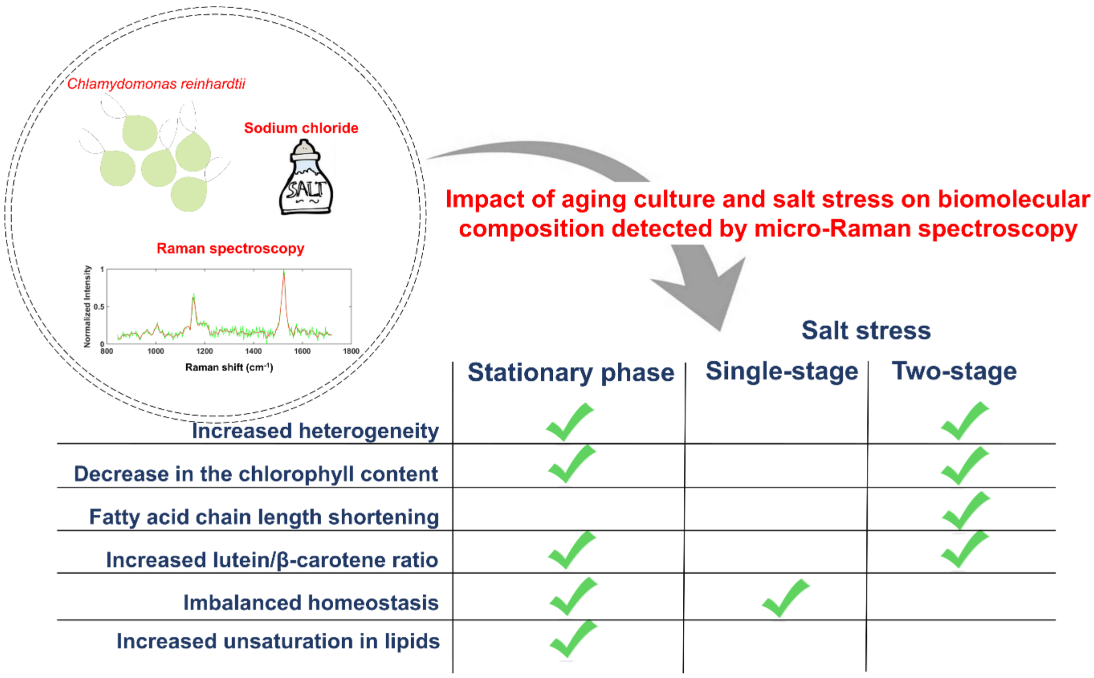

4 Developing the non-invasive use of micro-Raman spectroscopy for the determination of biomolecular composition in *Chlamydomonas reinhardtii*

4.1 Abstract

Microalgae are a rich source of carotenoids and lipids with enhanced yields during biotic or abiotic stresses. Using a non-invasive pigment profiling approach with micro-Raman spectroscopy, the effect of salinity stress on carotenoids and lipid composition was analyzed during the autotrophic growth of *Chlamydomonas reinhardtii* CC-125. Discrete wavelet transform (DWT) decomposition of Raman signal in different frequency bands, corresponding to lipids, starch, photosynthetic pigments, and proteins, was employed to enhance the signal-to-noise ratio and accuracy of peak center estimation. Raman spectral analysis of ν(C=C) mode indicated an increase in the carotenoids with lower conjugation length (lutein and zeaxanthin) compared to *β*-carotene, as the function of culture age and salinity stress especially when salinity stress was imposed in two-stage mode. Lipid C=C/C=O stretching and CH_2/CH_3 scissoring modes revealed heterogeneous subpopulations with different lipid profiles within the same culture, which gets enhanced under stress. Fatty acid chain length shortening as well as heterogeneous distribution of unsaturation content was observed under salt stress, especially under the two-stage condition. Population-scale heterogeneities in the carotenoid Raman mode peak center were highest during the stationary phase of the cultures and under salinity stress. Raman intensities could also successfully determine the correlations between the biomolecules and indicated hampered cellular stasis at the stationary phase of the culture. Interestingly, in all growth conditions, chlorophyll *a* Raman mode intensity was found to show a high correlation to that of *β*-carotene, pointing out a high degree of cooperativity in the light-harvesting complex pigments even during salinity stress. Although the Raman signal was obtained from a randomly selected small focal volume in the cell, a decrease in chlorophyll Raman mode intensities with age and salinity stress was well corroborated by single-cell population fraction measurements by microscopy. Thus, we demonstrate the usefulness of non-invasive pigment and lipid profiling with micro-Raman spectroscopy for developing an

optimization for conditions with high biomass yield and proper harvest time to obtain carotenoids with desired chemical composition and lipids of merit biofuel quality.

4.2 Introduction

Green microalgae have evolved through various generations as a promising source of energy feedstock, including biodiesel and nutraceuticals (Demirbas and Demirbas, 2011). While biodiesel is a downstream product of neutral lipids, nutraceuticals can be obtained from carotenoids (Dębowski et al., 2020) which are an integral part of the light-harvesting complex (LHC). Lipids, or more precisely the neutral lipids, i.e., triacylglycerols, accumulate in the form of droplets in the cytosolic region of green microalgae as a storage carbon reserve under stress (Walther et al., 2017). Environmental stress conditions like nutrient deprivation or excessive salinity induce the overproduction of these biochemicals, however, at the cost of poor cell survival (Cheng and He, 2014). Two-stage and gradient strategies have widely served as the alternate cultivation approach to increase feedstock productivity under salt stress (Aziz et al., 2020; Ali et al., 2021; Abomohra et al., 2020). In the microalgal biofuel industry, the quality of the product is equally important as its quantity (Kose and Oncel, 2017). These factors altogether constitute a multivariable scenario where screening an optimum condition for cultivation becomes the need of the hour.

Gas chromatography-based detection tools (GC-FID or GC- MS) constitutes the most desirable approach for quantifying the lipid content and determining the lipid composition. Widely used techniques to investigate pigment structure are X-ray crystallography, mass spectrometry, HPLC, circular dichroism, time-resolved fluorescence spectroscopy, electron microscopy, and light absorption (Drop et al., 2014; Dekker and Boekema, 2005; Liu et al., 2004; Natali and Croce, 2015). Most of these techniques require extraction and purification of bio-components in their native state from cells and demand high biomass. Moreover, extracted chlorophyll and carotenoids cannot retain their native structure, hence it is not possible to detect conformational changes. Also, detailed lipid composition is essential to learning the biofuel potential of the microalgal lipids, which is primarily dictated by the degree of unsaturation, the basis of all the biofuel quality parameters (Moser, 2009). Hence, there is a need to develop micro-scale optimization studies, which are non-invasive, fast, and high throughput.

Raman spectroscopy (RS) offers great potential for rapid, high throughput, multivariate and non-invasive analysis of lipid composition (Challagulla et al., 2016). The presence of Raman-active moieties in photosynthetic pigments enables the extraction of useful structural information from the unique fingerprint spectra falling between 700 – 1600 cm^{-1} (Wood et al., 2005), while the lipids are usually read in the wide region of 400 – 3000 cm^{-1} (Czamara et al., 2015). Raman spectroscopy (RS) has been widely used for the identification of the carotenoids present in photosynthetic micro-organisms, for example, peridinin in cyanobacteria (De Oliveira et al., 2015), siphonoxanthin in deep-sea green algae (Uragami et al., 2014) or the differential composition of β-carotene, lutein, and astaxanthin in flagellated and non- flagellated green microalgae (Osterrothová et al., 2019). Raman spectroscopy when used in the confocal geometry (micro-RS) further permits the acquisition of Raman data with high spatial resolution. Micro-RS data has been observed to correlate well with HPLC and GC-MS analysis (Osterrothová et al., 2019; He et al., 2017; Mehta et al., 2021). It even mitigates the problem of weak Raman signal, thus resulting in accurate localization and sensitive signal detection (Wei et al., 2014). With the help of micro-RS, the metabolic profiling and species classification of algal cells have become culture-free (Baladehi et al., 2021). In the past decade, micro-RS has emerged as a rapid biomolecular profiling tool in microalgal research, especially to study the lipid composition at the single-cell level (Wang et al., 2014; Jaeger et al., 2016; Wu et al., 2011). Additionally, it has also been used to check the effect of different stress variations on carotenoid composition, for example, the light-induced conformational changes in neoxanthin in green algae (Uragami et al., 2014), or heavy-metal stress in cyanobacteria (Nekvapil et al., 2021).

Salinity stress on microalgal cells is known to increase the carotenoid content (Paliwal et al., 2017), but the compositional or conformational changes as a result of stress imposition need detailed study. Micro-RS permits a label-free approach to simultaneously study multiple cellular metabolites and biomolecules such as starch, proteins, lipid molecules, carbohydrate levels, and carotenoid content (Huang et al.; Chiu et al., 2017; He et al., 2017). This approach of single-cell measurement allows tracking the single-cell phenotypic variability to reveal useful information lost in bulk measurements, which observe the mean of any variable. For example, effects due to a bimodal distribution, a broad distribution, or the presence of significant states in the tails of a probability distribution get ignored in bulk measurements (Altschuler and Wu, 2010). Although heterogeneity is inherent in cells due to noise in gene expression levels (Elowitz et al., 2002), it holds the key to a better understanding of the response of an organism to changing environmental conditions. However, despite the industrial importance, there are very few studies that focus on characterizing the heterogeneity and understanding the underlying distribution as a function of the stress in microalgae. Focusing more on the single-cell heterogeneity analysis could help improve the optimization of the microalgal culture protocols for good growth and biomass yield.

The work presented in this Chapter was aimed at using micro-Raman spectroscopy to identify population-scale compositional heterogeneities in lipid molecules and the photosynthetic pigments in *Chlamydomonas reinhardtii* CC-125 cells when exposed to salt stress. By deconvolution of the Raman spectra in the pigment fingerprint region, we decipher the associated changes in the carotenoid structure, produced under different modes of application of salinity stress, i.e., single-stage and two-stage application of 100 mM NaCl. The salt concentration of 100 mM caused no significant change in the growth characteristics of microalgae compared to the photoautotrophic control grown without any salinity stress, and therefore serves as the best cultural condition to optimize the Raman spectroscopic measurements. The measurements were performed at different stages of microalgal growth to understand the impact of stress along with the growth stages on the lipid profile and pigment composition of microalgae. Micro-RS was also used to predict the biofuel potential of microalgal lipids. Overall, the results emphasized the use of micro-RS in the multi-variate and non-invasive study of cellular homeostasis, lipid production, carotenoid composition, and detection of population-scale heterogeneities in lipid composition otherwise averaged out in bulk measurements.

4.3 Materials and Methods

4.3.1 Microalgal strain, growth media, and culture conditions

Chlamydomonas reinhardtii CC-125 was used as the model organism and the growth conditions were the same as mentioned in Chapter 2, Section 2.3.1. The salt stress was provided in two ways: single-stage and two-stage (as explained in the Section 2.3.2). Briefly, the single-stage cultures had 100 mM NaCl added at the beginning of culturing (SS 100). The two-stage cultures had 100 mM NaCl added in the early-log phase on the 2nd day of the culture (D2 100) and in the mid-log phase on the 4th day of the culture (D4 100). The *C. reinhardtii* cells were harvested on the 6th day (D6) and 10th day (D10), at the end-log and stationary phase, respectively (**Figure 4.1**).

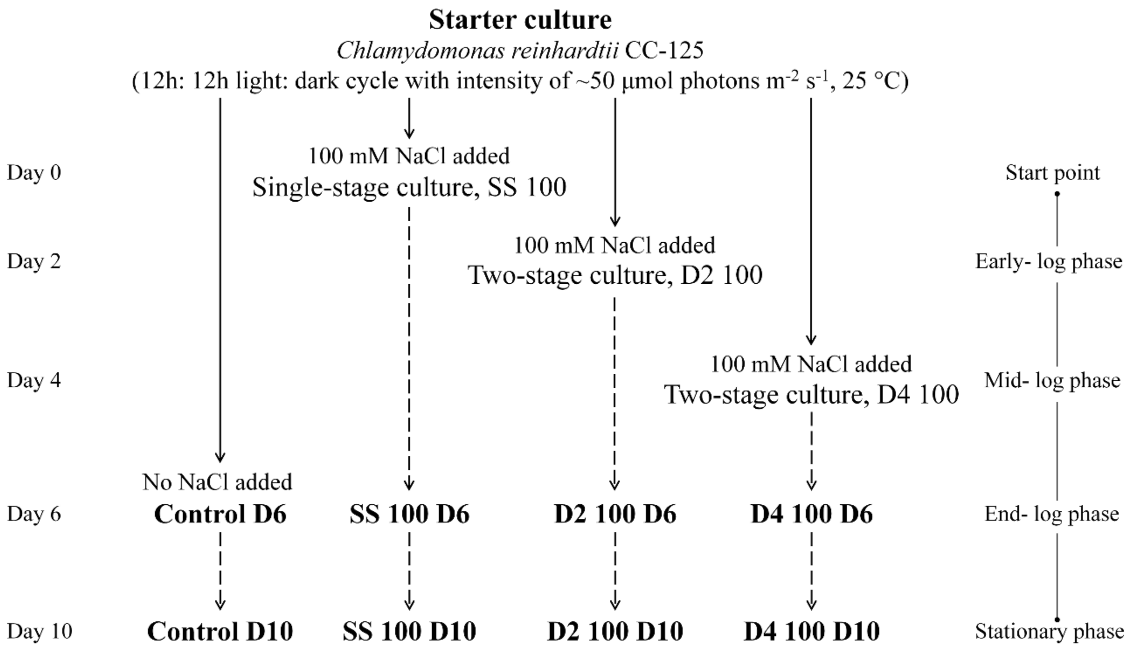

Figure 4.1. Tree diagram showing single-stage and two-stage strategies for salt stress.

C. reinhardtii cells grown in TAP medium without added salt are referred to as Control D6 and Control D10, depending on the day of sampling, i.e., day 6 (D6) and day 10 (D10), respectively. Similarly, culture treated at Day 0 with 100mM NaCl is referred to as SS 100 D6 and SS 100 D10; early-log phase salt-treated cultures are D2 100 D6 and D2 100 D10; mid-log salt-treated cultures are referred to as D4 100 D6 and D4 100 D10.

4.3.2 Micro-Raman spectroscopy of *C. reinhardtii* cells

C. reinhardtii cells grown under salinity stress were concentrated into a wet paste and air-dried on a clean glass slide (He et al., 2017). Raman spectral measurements were performed using a micro-Raman spectrometer (STR 300 series, AIRIX Corp., Japan) with an upright confocal geometry. A back-scattered Raman signal was collected through a 50X objective lens (NA= 0.6) with an incident beam of 50 mW power, attenuated by 5% with a neutral density filter from a 532 nm diode-pumped solid-state laser (Laser Quantum), A small focal volume was obtained from a spot of 500 nm. Rayleigh scattered light was eliminated with a holographic filter and the Stokes scattered light was passed through a grating of resolution = ~2.4 cm^{-1} in the fingerprint region, and detected by an Andor iDus EMCCD, cooled to -70 ºC. Two Raman spectral acquisitions, 2 s each (to maintain near single-cell conditions), were averaged and the instrumental background was subtracted to yield the final signal. A total of ~30 Raman spectra were captured from a single preparation of a culture. The spectrometer was calibrated using naphthalene as the standard, before data acquisition.

4.3.3 Signal processing of micro-Raman spectra

Each Raman spectrum was first normalized to correct for the incident intensity fluctuations arising from the scattering or absorption of the incident light, followed by background subtraction and de-trending by subtracting a polynomial best representing the background by a non-linear least-square fitting algorithm. The resultant data obtained after this pre-treatment had the same baselines and maximum peak intensity permitting a direct comparison of microalgal cells grown under different conditions. This pre-signal processing of the data was done using custom-made codes in MATLAB.

The pre-treated data was then processed using the discrete wavelet transform (DWT) algorithm which provided a fast-hierarchical scheme that passes a signal with length $L=2^n$ data points through a series of consecutive low-pass and high-pass filters, which decompose the signal into different levels or frequency bands. Symlet 4 wavelet was used with a level 2 decomposition, through the low pass and high pass filters providing outputs in form of approximation coefficients and detail coefficients, respectively. The data was decimated after this filter step by a factor of two per the Nyquist theorem. To decompose a signal with an optimal decomposition criterion, a signal of length $L = 2^n$

can be expanded in α different ways, where $\alpha \geq 2^{n/2}$ is the number of binary sub-trees of a complete binary tree of depth L. Since α is a large number, entropy-based (additive-type property) criterion, the classical Shannon entropy (non-normalized squared value of the logarithm of each signal sample) was found to be appropriate. The best wavelet decomposition tree was computed, and an appropriate threshold was selected for signal reconstruction.

4.3.4 Micro-Raman spectral data analysis

Heterogeneity in the Raman peak centers and intensity was analyzed using the Odds ratio (*OR*). using **Equation 4.1** for different stress conditions on day 6 and day 10 relative to the Control culture on day 6, where f_c = the fraction of the population of the Control culture at Day 6 with the Raman peak center the same as the median peak center, (1- f_c) = the fraction of population of the Control culture at Day 6 with Raman peak centers different from the median value of the population, f_s = fraction of population in a particular stress condition with Raman peak centers same as the population-scale median value, (1 - f_s) = fraction of population in a particular stress condition with Raman peak centers different from the population-scale median value. Since OR quantifies heterogeneities relative to a control, this is referred to as the heterogeneity index (HI).

$$OR = \frac{f_c/(1-f_c)}{f_s/(1-f_s)} = \frac{f_c(1-f_s)}{f_s(1-f_c)}$$

Equation 4.1. Odds ratio (*OR*)

Raman intensity fluctuations (I_f) were calculated as the ratio of the variance to the square of the mean (**Equation 4.2**), where σ is the standard deviation among the Raman intensity for ~30 cells, and *I* is the mean Raman intensity.

$$I_f = \frac{\sigma^2}{\langle I \rangle^2}$$

Equation 4.2. Raman intensity fluctuations (I_f)

The degree of unsaturation (DU) present in the fatty acid (FA) content of the cell was calculated as the ratio of Raman peak intensity of ν(C=C) and α(CH_2/CH_3) Raman modes ($I_\alpha = I_{\nu(C=C)}/I_{\alpha(CH2/CH3)}$). The fraction of saturated (SFA) vibrating at ~1440 cm^{-1} and unsaturated fatty acids (UFA) vibrating at ~1655 cm^{-1}, was also determined (Elizabeth et al., 2020). Other biofuel quality parameters like cetane number (CN) (Sarakatsanis, 2019), iodine value (IV, mg I_2 absorbed per 100 g of oil), and higher heating value (HHV, MJ kg^{-1}) was calculated based on DU. These calculations were run on three independent biological replicates. Error bars represent the standard deviation. The equations are as below:

$$\text{Cetane number (CN)} = 62.32 - 6.13 \times \text{DU}$$

Equation 4.3. Cetane number (CN)

$$\text{Iodine value (IV)} = 12.71 + 74.37 \times \text{DU}$$

Equation 4.4. Iodine value (IV)

$$\text{Higher heating value (HHV)} = 38.53 + 1.76 \times \text{DU}$$

Equation 4.5. Higher heating value (HHV)

Triolein and Microalgal oil (MA Oil) were used as experimental standards. Micro-Raman spectra were obtained for these standards and the degree of unsaturation (DU) was calculated, followed by the above-mentioned biofuel quality parameters. Triolein or the glyceryl trioleate was procured from Sigma-Y0001113 and MA Oil is the biofuel extracted from *Chlorella variabilis* (ATCC-PTA 12198) (Ghosh et al., 2015; Bhattacharya et al., 2016), tested and found to efficiently run vehicles.

4.3.5 Statistical analysis

Principal component analysis (PCA), statistical and ratiometric analysis of Raman peak intensities for lipid C–C, C=C, C=O stretching, and CH_2/CH_3 scissoring modes were performed using MATLAB R2015a. MATLAB was also used to generate normalized histograms of peak intensities to obtain the probability distribution of these quantities. Pearson's correlation coefficient among the cellular components, i.e., starch, protein, carotenoid, chlorophyll, and saturated and unsaturated lipids were calculated using MATLAB and the correlation matrix was constructed using customized Python codes on Google Colab. The coefficients were calculated for Raman spectra obtained from ~30 individual cells.

The reported values were derived from an average of three independent biological replicates, and the errors represent the standard deviation (S.D.). Statistical significance of the data was obtained by Student's t-test analysis performed in MS Excel, where the data was considered significant only if $p \leq 0.05$. The maximum significance of the data was obtained with $p \leq 0.0001$.

4.4 Results

4.4.1 Assignment of Raman modes to cellular biomolecules

To study the effect of salt stress on microalgal growth, lipid composition, and heterogeneity, micro-Raman spectra were acquired from ~30 individual cells belonging to each of the culture conditions. Raman signal collected from a single microalgal cell with a short acquisition time is usually very weak, due to scattering and absorption of the incident beam by the cytoplasmic matrix, extracellular media, pigments, or components of the cell wall. Moreover, cellular auto-fluorescence can result in a large non-uniform background too (Huang et al., 2010). As a result of these factors, the Raman scattered signal obtained from the cells is noisy, with a large, variable background. After appropriate background subtraction and normalization (section 4.3.3), a discrete wavelet transform (DWT) approach to denoise the noisy pre-treated data acquired for 2s was found to yield reproducible peak positions and centers. The 2-level decomposition achieved by DWT yields a typical approximation coefficient (a_2) along with the two detail coefficients (d_1 and d_2, non-decimated) as shown in **Figure 4.2B**. At this large accumulation time, even though noise is minimized due to signal averaging and whole-cell spectra can be obtained, long exposure to high laser power can alter the cellular dynamics resulting in erroneous results. Nevertheless, it gives a good estimate of the actual peaks present, which are deconvoluted with a Voigt function and peak centers accurately obtained. The DWT processed data were normalized to the strongest Raman peak (at around 1523 cm^{-1} corresponding to carotenoids) for each Raman data of the biological replicates for Control (no stress), SS 100 (single-stage, 100 mM NaCl stress), D2 100 (two-stage, 100 mM NaCl added on 2nd day of growth) and D4 100 (two-stage, 100 mM NaCl added on 4th day), all acquired on 6th day (end-log phase) (**Figure 4.3**). Raman signal acquired with 2 s acquisition time and subsequently DWT treated, illustrated enhanced accuracy in the peak center estimates after the DWT treatment (**Figure 4.4**). The normalized Raman signal was then used to analyze the fingerprint region in the wavenumber range of 850 – 1800 cm^{-1}, which revealed resolved contributions from various cellular constituents, such as photosynthetic pigments (chlorophyll and carotenoids), starch, proteins, and lipids. These peaks were deconvoluted with Voigt functions to obtain peak centers of the Raman bands chosen for study (**Figure 4.5**). The peaks identified after the transformation of Raman spectra with the DWT denoising algorithm accurately match previous estimates of Raman peaks observed for the biomolecules under study (Czamara et al., 2015; Wiercigroch et al., 2017; Rygula et al., 2013; Wood et al., 2005) as well as for *Chlamydomonas* sp. (He et al., 2017) (**Table 4.1**). The strongest peak corresponds to the C=C stretching mode of carotenoids in the region of around 1523 cm^{-1}, but a spectral deconvolution of this peak reveals two prominent peaks (**Figure 4.5**), one centered around 1520 cm^{-1} (car-i), the second peak center occurs in the range 1526 cm^{-1} - 1532 cm^{-1}. The other prominent carotenoid modes are C−C stretching around 1150 cm^{-1} (car-ii) and C-CH_3 deformation/stretching around 1006 cm^{-1} (car-iii). Chlorophyll Raman peaks are much weaker than carotenoid peaks and lie about 1186 cm^{-1} (chl-i), 964 cm^{-1} (chl-ii), and 1289 cm^{-1} (chl-iii). Carotenoids give a strong Raman signal due to pre-resonant enhancement with a 532 nm excitation laser (carotenoid absorption band) (Zajac et al., 2017). This negates the need for surface enhancement of the Raman signal and makes Raman spectroscopy a very sensitive tool for the exploration of carotenoid structure and composition in microorganisms, as has been demonstrated by recent studies (Jehlička et al., 2014). The other peaks are assigned to starch at 864 cm^{-1}, lipid at 1063, 1086, 1440, 1656, and 1750 cm^{-1}, and proteins at 1349 cm^{-1}. A drawback of this DWT denoising algorithm is that the data are down-sampled, but this did not obscure the signal integrity and accuracy of the above main Raman peaks (**Figure 4.6**) also mentioned in **Table 4.1**. In the following sections, Raman modes around these wavenumbers are further explored across individual cells.

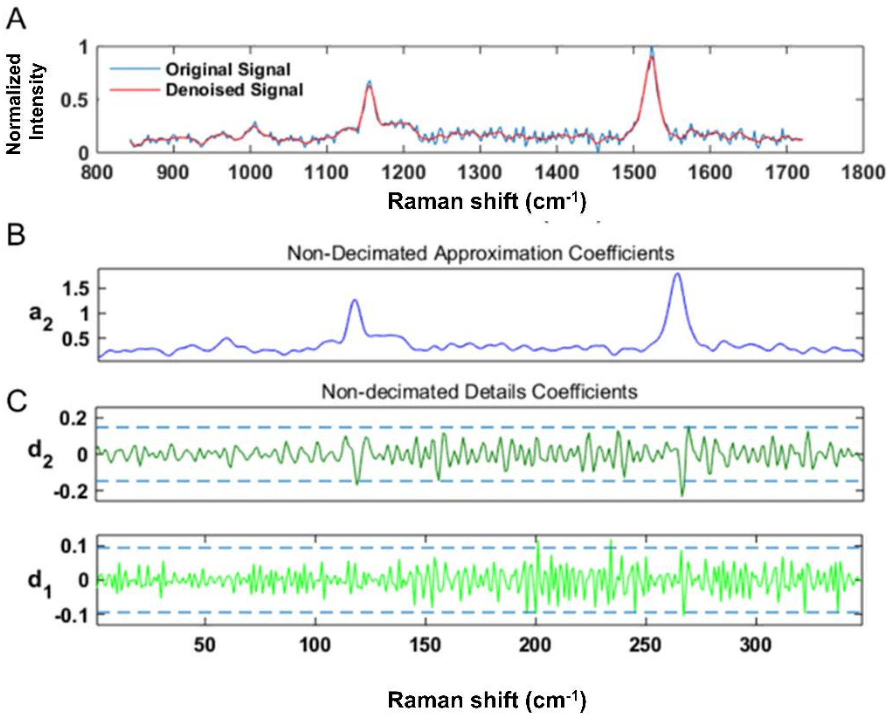

Figure 4.2. Discrete wavelet transform (DWT) denoising of the Raman signal.

A. The signal (blue curve) is decomposed into different frequency bands. **B**. The output of the low pass filter is the approximation coefficient (a_2) and that of the high pass filter are the details coefficients (**C**, third and fourth panel). Since a two-level decomposition was performed, only the detail coefficients d_1 and d_2 are shown. The denoised signal is shown as a red curve on the noisy blue data (**A**).

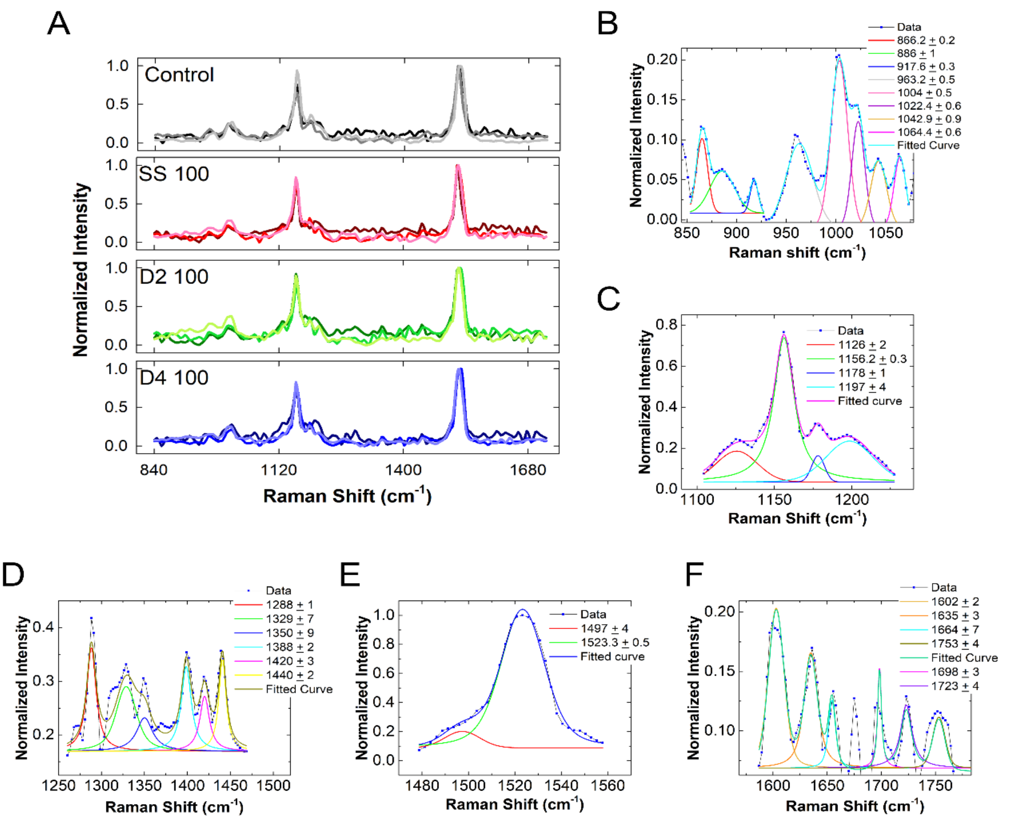

Figure 4.3. Deconvolution of the Raman spectra of *C. reinhardtii* cells yields distinct Raman peaks.

A. Overlay of denoised Raman spectra across three biological replicates each of Control (no NaCl), SS 100 (100 mM NaCl added on Day 0), D2 100 (100 mM NaCl added on Day 2), and D4 100 (100 mM NaCl added on Day 4 of culture) captured on Day 6 of growth. The Raman spectra obtained for Day 10 samples were similar to that of Day 6 and hence not shown here to avoid repetition. **B-F**. The Raman spectra were smoothened and fitted with the Voigt function, as shown in each graph. Deconvolution revealed Raman peaks with standard error values mentioned in the legend box of each graph. The main peaks used in the present study are 866 cm^{-1} and 1064 cm^{-1} (**B**), 1156 cm^{-1} (**C**), 1288, 1350 and 1440 cm^{-1} (**D**), 1523 cm^{-1} (**E**), and 1664 and 1753 cm^{-1} (**F**).

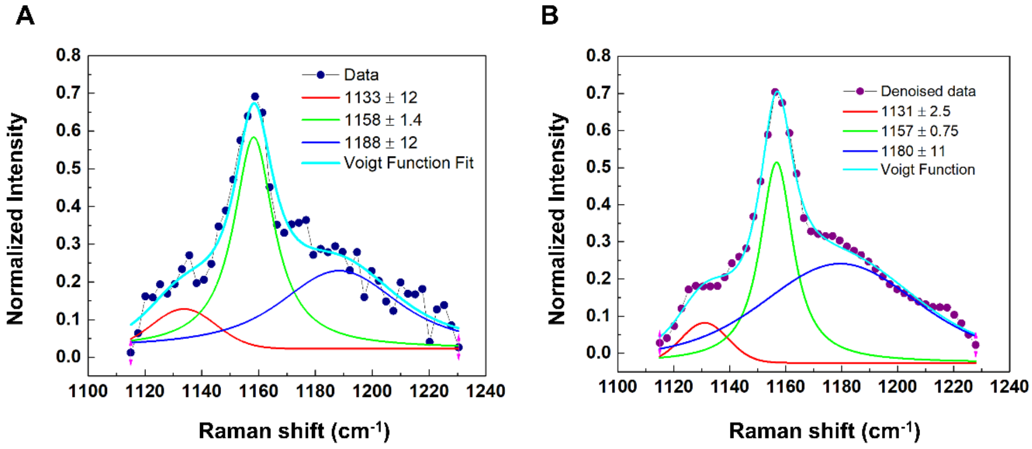

Figure 4.4. Representative peak centers of background-subtracted Raman signal before and after denoising.

A. A peak from the noisy Raman data acquired with 2 s integration time (Control Culture Day 10) is deconvoluted with a Voigt function into three peaks with peak centers as given in the legend. **B**. The same data, but denoised, and the same peak is fitted to a Voigt function. The peak centers of DWT denoised data show improved accuracy in peak center estimates.

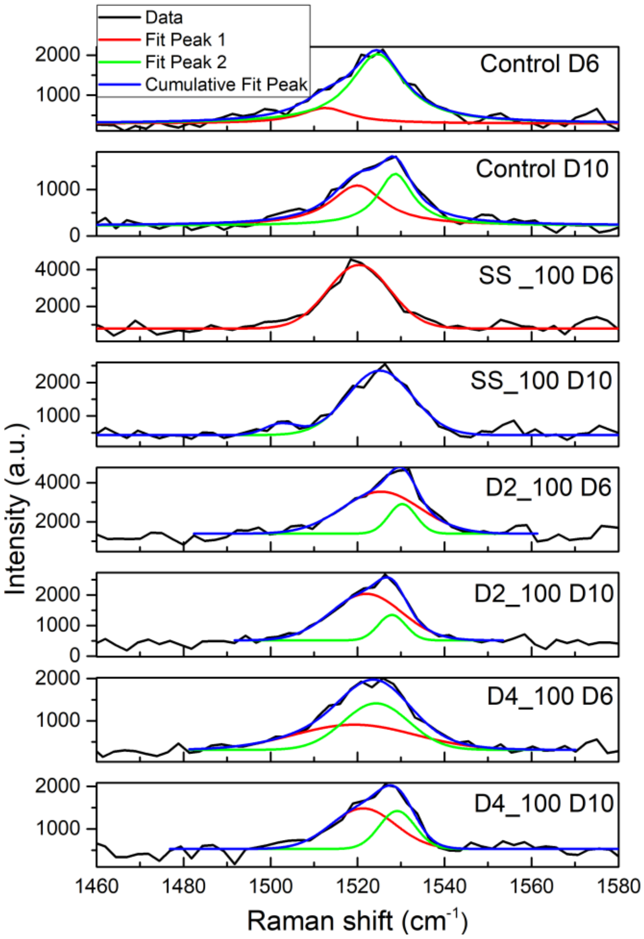

Figure 4.5. Deconvolution of the carotenoid peak at 1523 cm^{-1}.

Representative single-cell peaks for the most intense carotenoid peak corresponding to the C=C stretching mode (car-i). The main peak is deconvoluted into two peaks, one with a peak center around 1520 cm^{-1} (Peak 1, marked in red) and the other peak centered around 1530 cm^{-1} (Peak 2, marked in green).

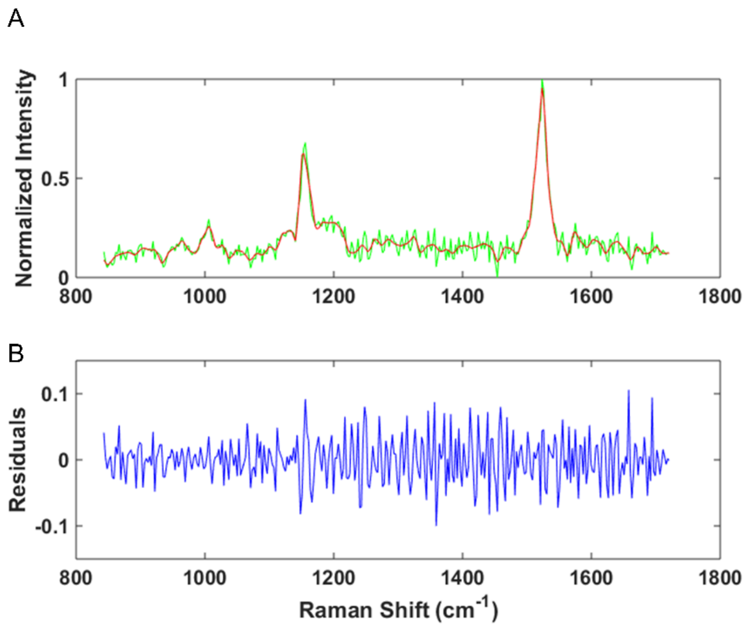

Figure 4.6. Signal integrity and accuracy post-DWT treatment of the Raman spectra of *C. reinhardtii*.

A. A typical background-subtracted data for Control D6 is shown as the noisy green curve. The red curve is the result of using the DWT algorithm for denoising. **B**. The residual plot of the DWT denoised data for the background-subtracted data represents randomly distributed points across the fit.

Table 4.1. Raman peak assignments of starch, protein, chlorophyll, carotenoid, and lipids for *C. reinhardtii*.

Raman shift (cm^{-1})	Component	Peak assignment	Reference
~864	Starch	C–O–C stretching and ring breathing modes in amylopectin and amylose units of starch	(Wiercigroch et al., 2017; He et al., 2017)
1350	Protein	C–Cα–H bending and Cα–C stretching in α-helix or amide I and III regions of tryptophan	(Rygula et al., 2013)
~1064	Lipids	C–C stretching	(Czamara et al., 2015; He et al., 2017)
~1440		Scissoring of CH_2/CH_3 bond	
~1656		C=C stretching	
~1750		C=O stretching	
1519-1530 (car-i)	Carotenoids	carotenoid stretching mode ν(C=C)	(Wood et al., 2005)
~1156 (car-ii)		*β*-carotene stretching mode ν(C-C)	
~1006 (car-iii)		*β*-carotene stretching mode ν(C-CH_3)	
~1186 (chl-i)	Chlorophylls	CH in-plane blend, N-C stretch, chlorophyll *a*	
~964 (chl-ii)		C-C-C /N-C-C in-plane bend of chlorophyll *a*	
~1289 (chl-iii)		chlorophyll *a*	

4.4.2 Validation of the Raman peak intensity with Nile red fluorescence representing the lipid production in *C. reinhardtii* cells under salt stress

Raman laser spot size under the current experimental conditions is ~500 nm, which is 1/20th part of the cell (Chlamydomonas is ~10 μm in diameter). To find out the reliability of the observed Raman intensities in representing the total content of the component from such a small focal spot of the cell under study, it was important to compare the Raman data with data acquired through biochemical or other approaches. Raman band at 1063 cm^{-1} (C-C stretch of lipids) was chosen to analyze lipids because the peak center of this band shows minimum fluctuations across different growth conditions (Appendix A3). The intensities of the 1063 cm^{-1} peak were compared to the absolute neutral lipid concentration in *C. reinhardtii* obtained from Nile red fluorescence intensity measurements by epifluorescence imaging of stained lipid droplets in about 100 cells, and the fluorescence intensity per area of the cell was estimated using Fiji software (Section 2.3.7 and **Figure 2.14**). The Raman intensity at 1063 cm^{-1} is observed to be normally distributed for all growth conditions, similar to the single-cell Nile red fluorescence intensity distributions which fit either normal or log-normal distributions (**Figure 4.7**). The average Raman and the fluorescence intensities of one cell are a good presentation of the total lipid content of the cell. The gray-colored dashed lines in **Figure 4.7** represents the net lipid content of the population, which is shown to undergo red-shift compared to the Control in salt stress conditions, in both Raman and fluorescence measurement. The net lipid content is observed to increase substantially in both fluorescence and Raman measurement as an effect of the salt stress and decreases on day 10 as compared to day 6 (**Table 4.2**). In addition, the standard deviations, represented by the pink-shaded region in each graph, also increase under stress as compared to Control for both the Raman and Nile red fluorescence intensity distributions. The standard deviation is a good measure of the heterogeneity of the distribution which is observed to increase under salt stress. Moreover, in both Raman and Nile red measurements, the distributions have similar kurtosis (a measure of the “tailedness” of a probability distribution of a random variable) for Control to start with, but show large deviations from the Control culture distributions, especially in two-stage. Despite accumulating vibrations from a small focal spot of the cell, Raman measurement serves as a reliable tool for both small-scale absolute and relative single-cell lipid quantifications in microalgae under stress.

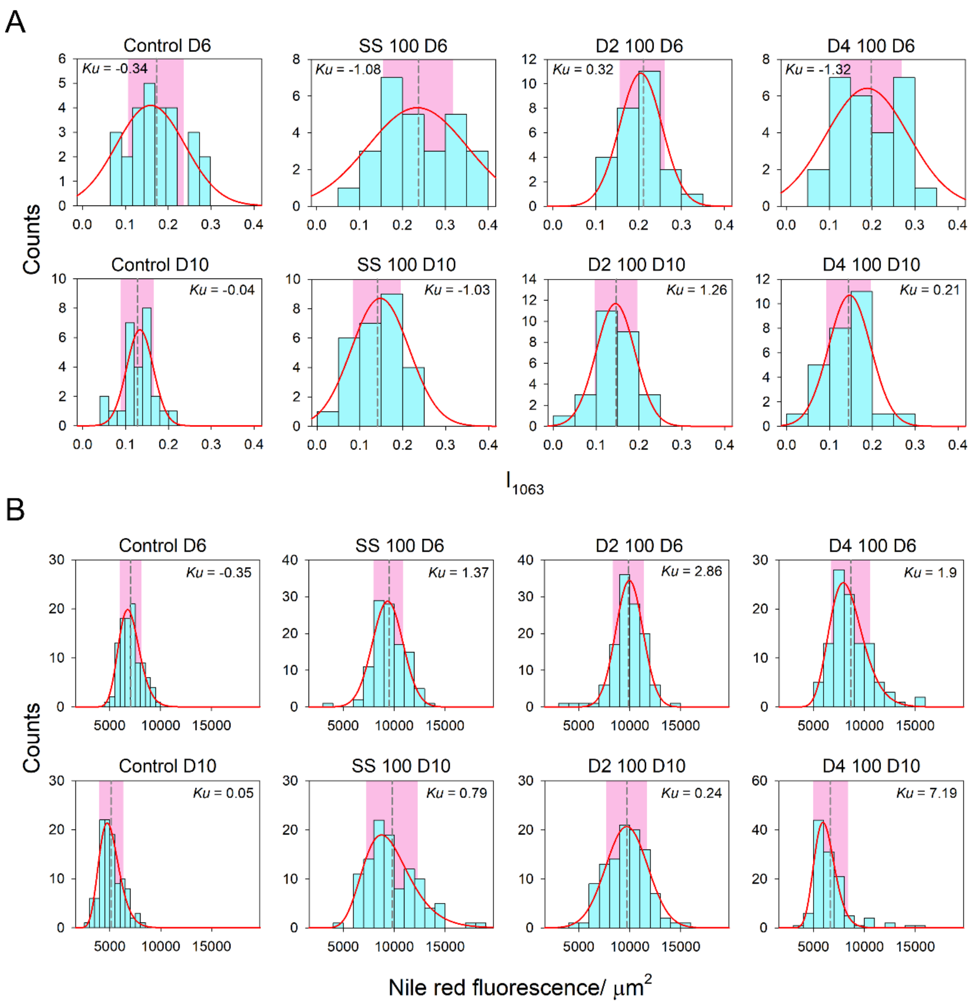

Figure 4.7. Probability distribution of lipid molecules in *C. reinhardtii* cells under salt stress measured by Raman spectroscopy and fluorescence microscopy.

A. Distribution of ν(C–C) $_1$ vibration as measured by Raman spectroscopy at 1063 cm^{-1} representing ~ 30 cells. **B**. Probability distribution of Nile red fluorescence depicting neutral lipid droplets per area of the cell (μm^2) measured for ~ 100 cells. The red curve represents the fitted distribution. Gray-colored dashed line is the data average spanned on each side by the experimental standard deviation (highlighted with pink background). Ku is the kurtosis.

Table 4.2. Mean Nile red fluorescence intensity and normalized Raman intensity measured at 1063 cm^{-1} across a population of ~100 *C. reinhardtii* cells.

Growth condition	Mean fluorescence intensity	Mean normalized Raman intensity at 1063 cm^{-1}
Control D6	7053	0.173
SS 100 D6	9514	0.238
D2 100 D6	9883	0.211
D4 100 D6	8670	0.198
Control D10	5119	0.128
SS 100 D10	9796	0.141
D2 100 D10	9691	0.147
D4 100 D10	6657	0.144

4.4.3 Biomolecular correlation analysis by Raman spectroscopy in *C. reinhardtii* under salt stress

Earlier in this study, we observed that sodium chloride at 100 mM concentration increases the starch and lipid production in *C. reinhardtii* (**Figure 2.9 Figure 2.10**). It causes a significant increase in the cell size during the log phase of the culture followed by a reduction during the stationary phase (**Figure 2.15**). It also deteriorates cell circularity (**Figure 2.16**). However, there is an insignificant impact on the cell density at 100 mM NaCl (**Figure 2.4**). These results signify that 100 mM NaCl is still below the threshold concentration to cause salt stress-induced osmotic damage to the cells. It would be interesting to study how various cellular bio-components *viz*. starch, chlorophyll, carotenoids, proteins, and lipids are correlated to each other at one time inside the cell. We studied the correlation between these bio-components using the corresponding Raman intensities (**Table 4.1**). Pearson's correlation coefficients are mentioned in Appendix A4. The relative changes in different biomolecules are evident from Pearson's correlation matrix (**Figure 4.8**). The correlation matrices show the overall negative correlations on day 10 in contrast to day 6. The correlation coefficients for the Control culture remain unchanged over the growth cycle of the organism. Single-stage salt stress exhibits more negative correlations in comparison to two-stage cultures. Deteriorating correlation values on day 10 suggest poor growth in the stationary phase.

There is a strong negative correlation between carotenoid-starch and carotenoid-lipid observed under all conditions. Chlorophyll-starch and chlorophyll-lipids are the correlations that become more negative under salt stress on day 10. This is also accompanied by hampered protein-lipid and starch-lipid inter-relations, the former being more pronounced in the single-stage while the latter in the two-stage. The Raman intensities, however, are captured within cellular volume at the scope-focal point, and are not indicative of the biomolecules in the entire cell. Despite this analysis, it may be understood that the cellular distribution of different biomolecules under study is disturbed under salt stress and varies as a function of the mode of salt stress application. The results demonstrate that Raman intensity correlations are sensitive to the age and salt stress condition of the culture and can be a rapid assay to determine the physiological state of cells under stress relative to an appropriate control.

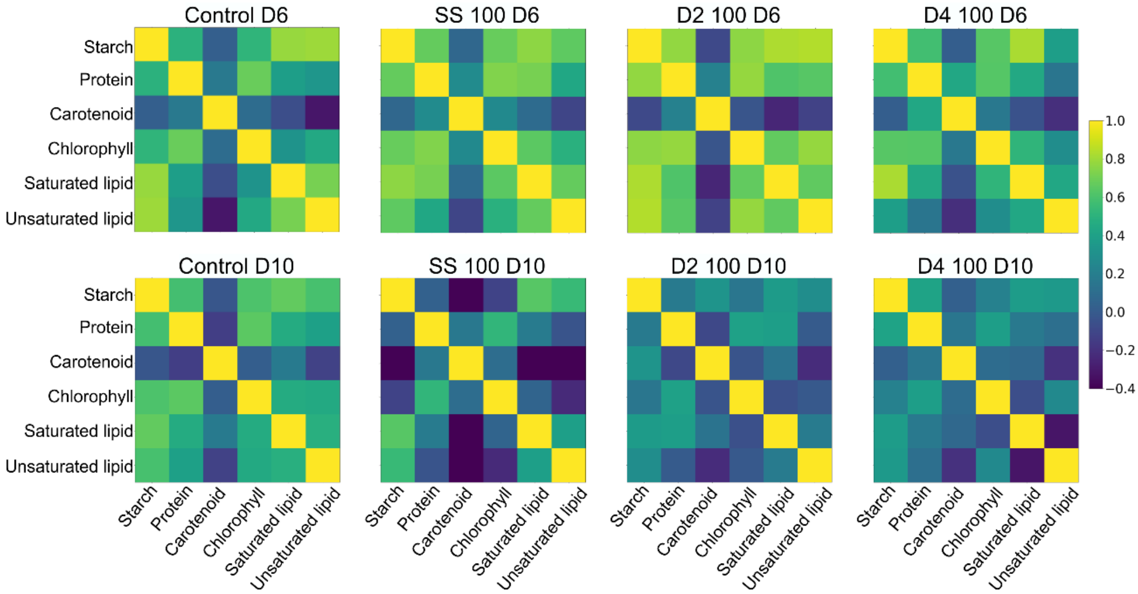

Figure 4.8. Correlation matrix of the cellular components of *C. reinhardtii* cultivated under different modes of salt stress.

Pearson's correlation coefficients were calculated for cellular components- starch, protein, carotenoids, chlorophyll, saturated lipid, and unsaturated lipid for ~ 30 cells each from the different cultivation conditions labelled at the top of each panel using the nomenclature mentioned in the text. The color scale ranges from Yellow (correlation coefficient = 1, highest positive correlation, assigned for self-correlation) to Blue (correlation coefficient = -0.4, the highest negative correlation observed).

4.4.4 Chemical composition and population distribution heterogeneities of carotenoids and chlorophyll in *C. reinhardtii* under salt stress

4.1.1.1 Carotenoid chemical composition heterogeneities

It is evident from **Figure 4.5** that the carotenoid stretching mode ν(C=C) arises due to a contribution from different carotenoids present in the cells because the peak is broad and can be deconvoluted into two major ν(C=C) modes, one at 1520 cm^{-1}, and the other around 1526 cm^{-1} - 1532 cm^{-1}, and this latter mode sensitively depends on the growth conditions and growth phase of the culture. Detailed analysis of the Raman peak centers for carotenoid modes reveals heterogeneities in the Raman spectra acquired for ~30 cells for different growth conditions (**Figure 4.9**). These heterogeneities are quantified with the help of heterogeneity indices (HI) values. In the case of car-i mode, peak shifts to higher wavenumbers are observed for a large fraction of cells in Control D10, SS_100 D10, and D2_100 D6 (**Figure 4.9A**). Since this peak depends on conjugation length, an increase in peak center wavenumber means the production of more carotenoids with lower conjugation length than the composition corresponding to the median value of 1526 cm^{-1}. In D2_100 D6, the median value is observed at 1529 cm^{-1}. The carotenoid composition heterogeneity in D4_100 is observed to be less, with heterogeneity indices even lower than in the Control culture. The highest HI values thus occur for Control D10, SS_100 D10, and D2_100 D6 (**Figure 4.9D**). In the case of car-ii mode, except D2_100 D6 and D4_100 D10, which show median peak center values at 1159 cm^{-1} and 1153 cm^{-1} respectively, all other cultures show peak center median values at 1156 cm^{-1}. However, the HI values are highest for SS_100 D10 and D4_100 D10 (**Figure 4.9B and E**). For car-iii, large heterogeneity is observed in Control D6 itself (**Figure 4.9C and F**). Hence, HI values differ between different cultural conditions. Overall, the shift in peak centers was observed in all the Raman modes of carotenoids. The shift signifies the occurrence of compositionally different carotenoids in the salt stress-exposed cells.

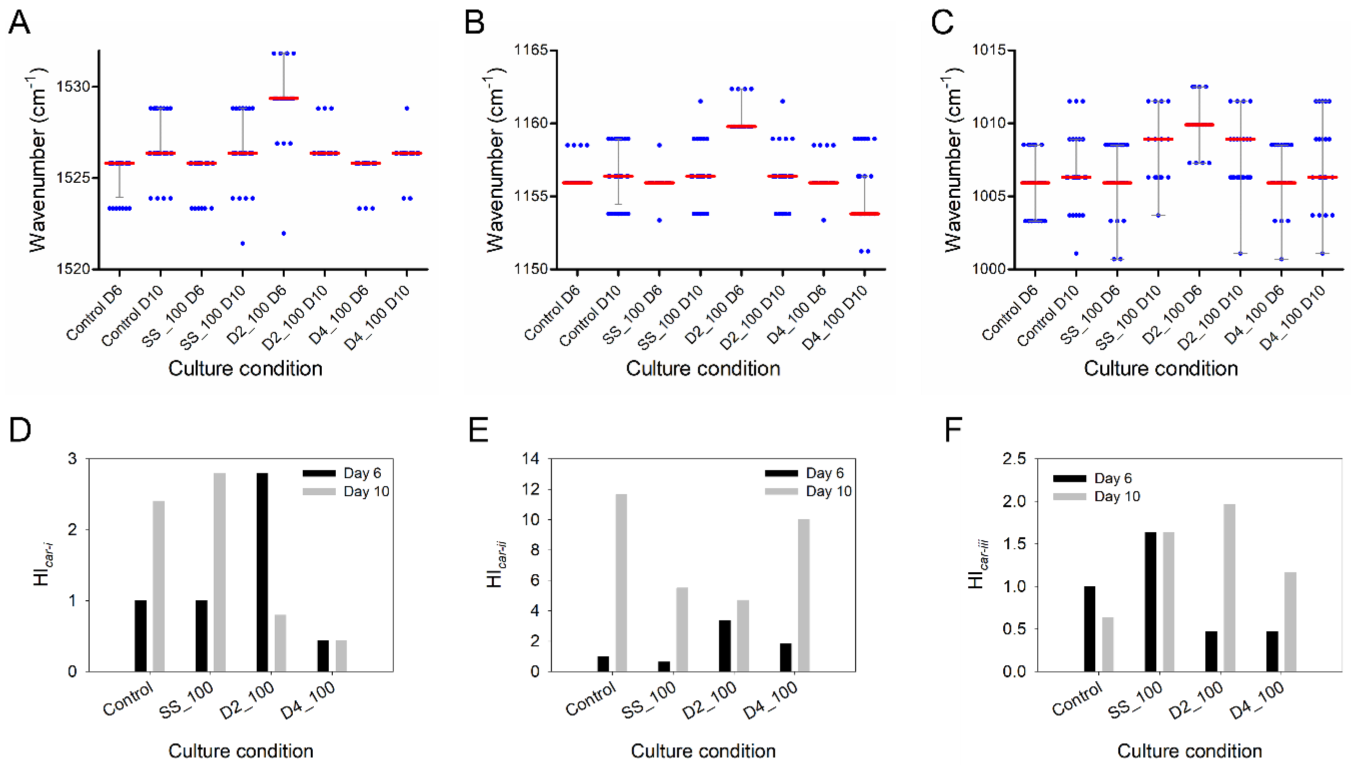

Figure 4.9. Heterogeneities in carotenoid chemical composition in *C. reinhardtii* under salinity stress as represented by the Raman peak positions.

A, B, and C. Heterogeneities in peak center position in wavenumber of carotenoid modes, car-i, car-ii, and car-iii, respectively, ν(C=C), as a function of mode of application of salinity stress and age of culture. The median values are shown in red. The gray-colored bars represent the interquartile range. The car-i mode shown is the peak center corresponding to the maximum of each convoluted peak. **D, E, and F**. Heterogeneity indices (HI) in peak center position of carotenoid mode car-i, car-ii, and car-iii, respectively, as a function of mode of application of salinity stress and age of culture.

4.4.4.2 Distribution and inter-relation of intensities of carotenoids and chlorophyll Raman modes with age and mode of application of salinity stress

Based on the deconvolution of the C=C stretch of carotenoids (**Figures 4.5 & 4.9**), two Raman modes were obtained, one at 1520 cm^{-1} corresponding to β-carotene, and the other observed at higher wavenumbers (1528- 1532 cm^{-1}) correspond, respectively, to zeaxanthin and lutein. The Raman intensity of lutein/ zeaxanthin modes acquired from ~30 cells has a Gaussian probability distribution with a finite spread, as shown in **Figure 4.10**. While the intensity distributions remain unchanged in Control and SS_100 with the age of culture, a shift to lower values with the age of culture is observed in D2_100. In D4_100, the intensity distribution is very broad at D6, but the standard deviation is lower than the control. A single Raman mode intensity is susceptible to instrumental drifts, fluctuation in incident laser intensity, and other external factors. Therefore, the ratio of the peak intensity at the median peak center for the C=C stretch (car-i) to the peak intensity of the C-C stretch of β-carotene (car-ii) for different growth conditions was studied. This represents the ratio of lutein/ zeaxanthin to β-carotene in the observed focal volume in the cells. This ratio was observed to remain unchanged with the age of culture in Control and SS_100, whereas, in D2_100 and D4_100, lutein/ zeaxanthin content increased to β-carotene with increasing age of culture.

Since carotenoids are closely associated with chlorophylls in the LHC, it becomes necessary to study the effect of salinity stress on chlorophyll pigments. Relative changes in chlorophyll to carotenoids were obtained with the help of peak intensity ratio probability distributions of the chlorophyll mode (chl-iii), centered around 1289 cm^{-1}, to that of the car-i mode in a spectrum. These probability distributions are shown in **Figure 4.11**, for different culture conditions on day 6 and day 10. The most remarkable feature of the distributions is the decrease in the spread of distributions with the increasing age of the cultures. Interestingly, the SS_100 condition has a bimodal intensity distribution on day 6, the exponential phase, which becomes mono-modal on day 10, the stationary phase. The mean values represented as a dashed line in **Figure 4.11** shift towards the lower values at day 10 in all cases, except the control. To investigate the reason for this decrease in the Raman peak intensity, bright-field imaging of *C. reinhardtii* cells was carried out for all growth conditions, and representative images are shown in **Figure 4.11B**. It is evident from these images that there is a marked decrease in the chlorophyll content of the cells under salinity stress (green-colored regions), and a shrinkage of the cup-shaped chloroplast with culture age. In D4_100 at day 10, cells without any chlorophyll are observed. The estimation of the fraction of cells containing chlorophyll in an ensemble of around 125 cells revealed a noticeable decrease at day 10, the stationary phase, for all conditions. These results point to the fact that the intensity of the car-iii mode is positively correlated to the chlorophyll content in the cells. Moreover, although these estimates were obtained for a small focal volume, a random sampling of pigment Raman mode intensities in small focal volumes for a large number of cells leads to probability distribution estimates which can be used for non-invasive chlorophyll quantification in cells, as evident after comparison with single-cell bright field microscopy images.

The probability distribution analysis of chlorophyll *a* (chl-iii at 1289 cm^{-1}) is based on the ratiometric intensities, obtained relative to the most intense peak for carotenoid mode belonging to β-carotene (car-i) at ~1520 cm^{-1}. Hence, it was worthwhile to analyze the interrelation between the chlorophyll and carotenoid Raman peak intensities when *C. reinhardtii* cells are subjected to salinity stress. Interestingly, all culture conditions except SS_100 on day 6 show positive correlation coefficients with values above 0.5 (**Figure 4.12**). On day 10 of the culture growth, the correlation between the population-scale intensities of chl-iii and car-i for SS_100 increases. This demonstrates high cooperativity among the chlorophyll and carotenoid molecules in the LHC regardless of the mode of application of salinity stress and age. Although the decrease in chlorophyll content is observed in cultures exposed to salinity stress in the stationary phase of growth, the chlorophyll-carotenoid coordination is maintained, thereby protecting the photosynthetic apparatus. Furthermore, intensity fluctuations in these Raman modes reveal higher I_f values for both chlorophyll and carotenoid under salinity stress (**Figure 4.13**). The highest fluctuations are observed on day 6, for carotenoids in SS_100 and chlorophyll in D4_100. Therefore, salinity stress not only results in changes in the carotenoid composition but also increases population-scale variations in the pigment content observed in the focal volume. The distribution of these Raman mode intensities obtained from sampling several cells can give a better idea of average pigment content. However, a study of the interrelation of Raman mode intensities of pigments in the focal volume in each cell gives information about the relative changes induced in the pigments as a consequence of salinity stress, evident from **Figure 4.12**.

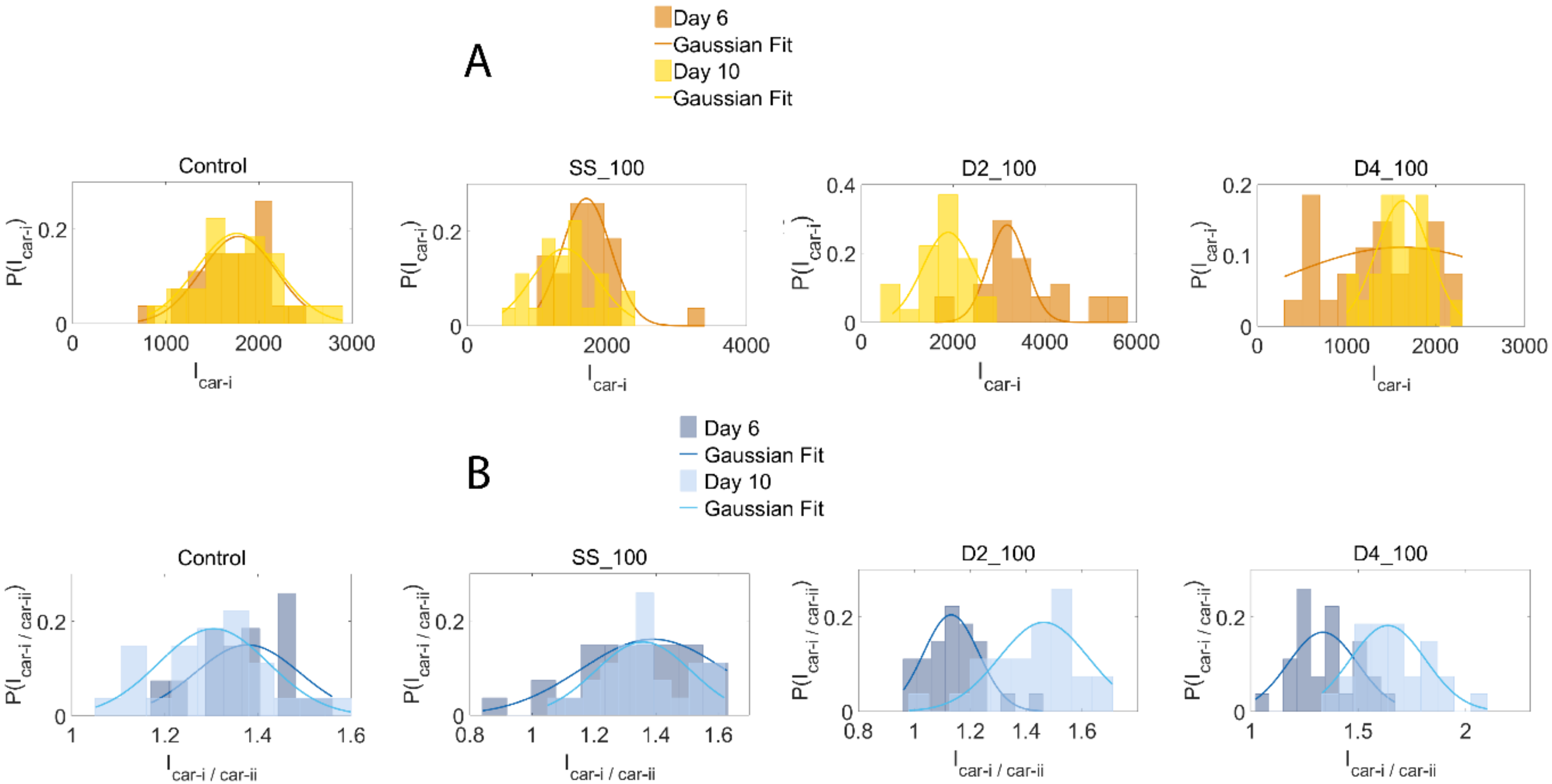

Figure 4.10. Population-scale probability distribution of peak intensity obtained at peak center corresponding to carotenoids in *C. reinhardtii* under salinity stress.

A. Probability distribution of Raman intensity of the carotenoid C=C stretching mode (car-i) corresponding to the median values obtained for different modes of salinity stress at day 6 and day 10 of growth. **B.** Probability distribution of the ratio of the peak intensity of the C=C stretching mode corresponding to the median values (from **Figure 4.9**), obtained upon deconvolution, to the peak intensity of the C-C stretching mode corresponding to β-carotene (**Table 4.1**), shown as a function of mode of cultivation and age of culture.

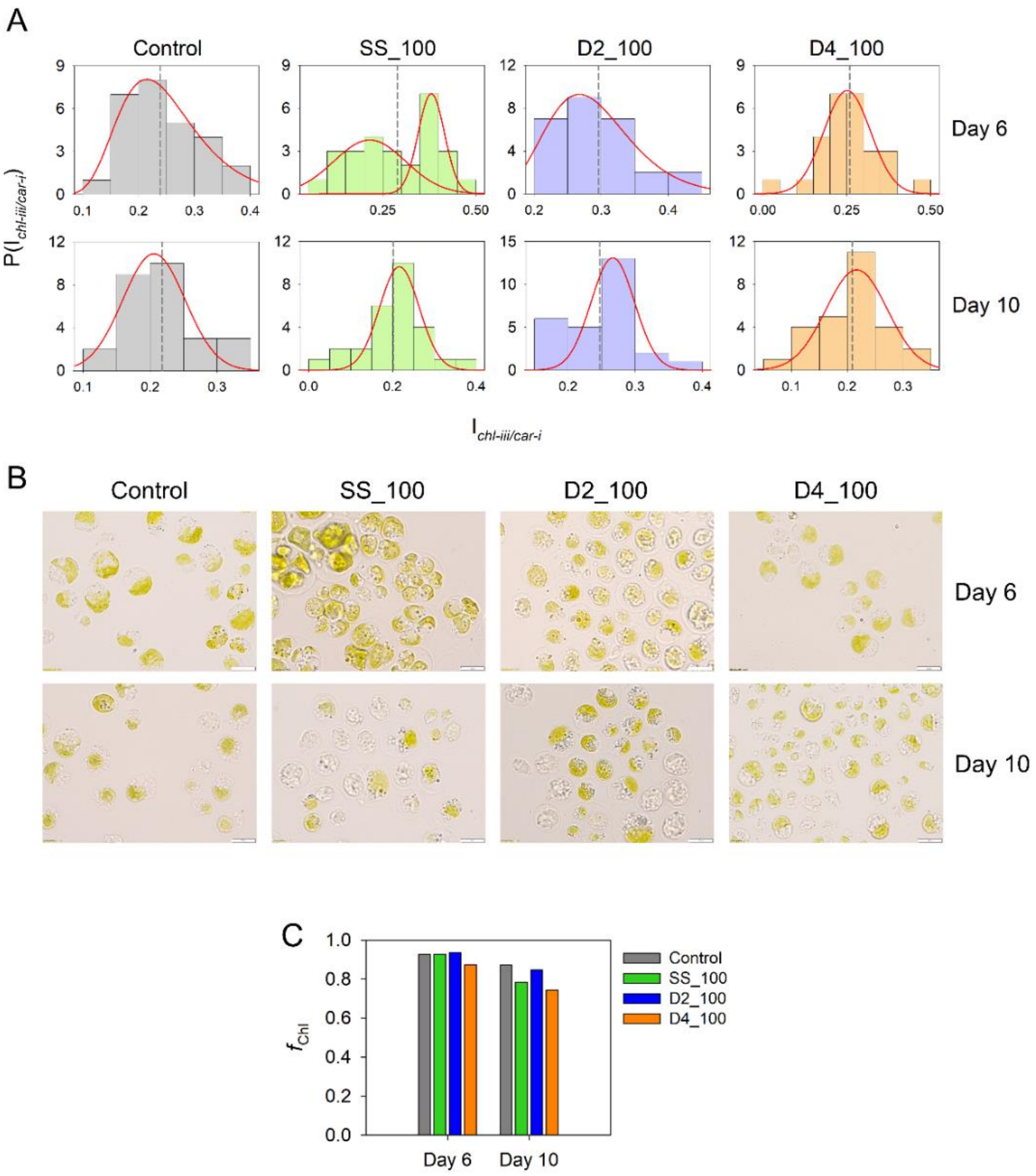

Figure 4.11. Changes in Raman scattering intensity of chlorophyll mode in *C. reinhardtii* under salinity stress.

A. Distribution of Raman intensities of the ratio of chlorophyll-*a* mode, i.e., chl-iii to the carotenoid mode, car-i, for different modes of salinity stress at day 6 and day 10 of culture growth, plotted as a function of intensity ration ($I_{chl\text{-}iii/car\text{-}i}$). The dashed lines represent the mean values of each distribution. **B.** Representative bright-field images of cells for different cultivation conditions on day 6 and day 10. The green color appears due to the presence of chlorophyll in the cup-shaped chloroplast. **C.** Fraction of cells in a total population of 125 cells containing chlorophyll on day 6 and day 10 for cultures grown under different conditions.

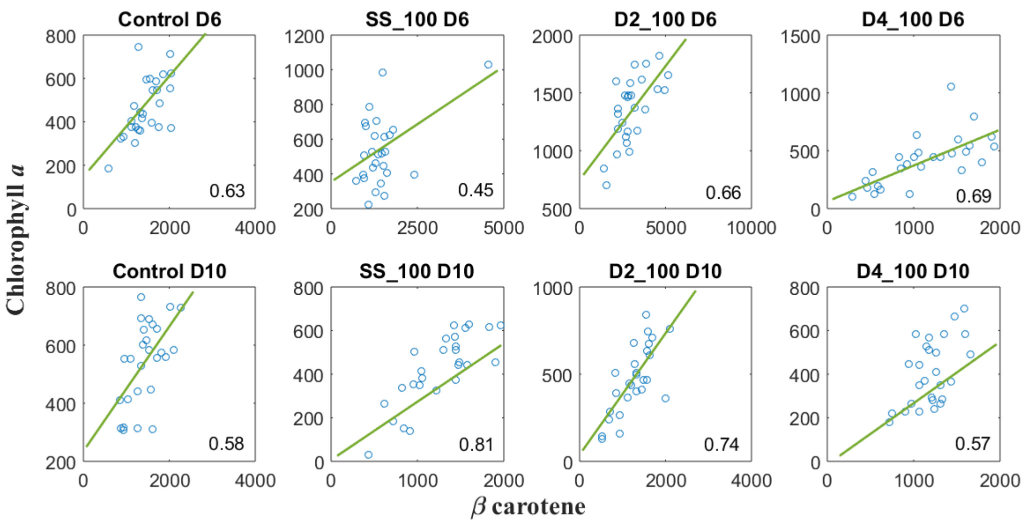

Figure 4.12. Pearson's correlation of chlorophyll and carotenoid as obtained from Raman modes in *C. reinhardtii* under salt stress.

Correlations between the population scale intensities of chlorophyll a mode (chl-iii) at 1289 cm^{-1} and the β-carotene C=C stretching mode (car-i) at 1520 cm^{-1} as a function of mode of cultivation under salinity stress and age of the culture. The Pearson's correlation coefficient for each pair is given in the bottom right corner of each graph.

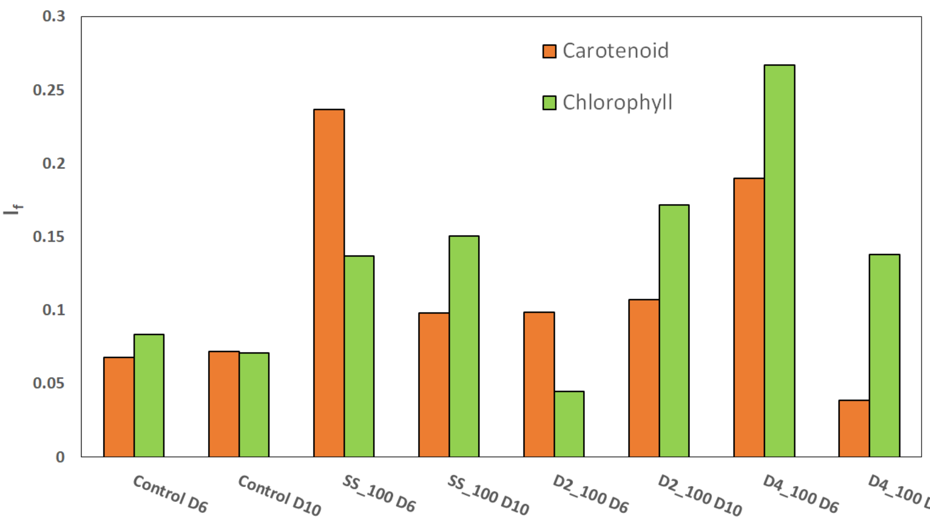

Figure 4.13. Intensity fluctuations of Raman modes of chlorophyll and carotenoids obtained in *C. reinhardtii* under salt stress.

Raman scattering intensity fluctuations (I_f) from modes corresponding to the β-carotene C=C stretching mode (car-i) at 1520 cm^{-1}) and the chlorophyll a mode (chl-iii), calculated for ~30 cells of each culture condition on day 6 and day 10.

4.4.5 Characterization and distribution heterogeneities of lipids produced by *C. reinhardtii* under salt stress

4.4.5.1 Biofuel quality of lipids

In the biofuel industry, increasing lipid productivity and producing biofuel of commercial quality are among the most essential requirements for maximizing profit. Biofuel quality is determined by the length of the carbon chain and degree of unsaturation (DU) of FAs, which decide the cetane number (CN). The average DU values for different culture conditions were calculated with ratiometric analysis, as the ratio of Raman peak intensity at C=C stretching ($I_{\nu(C=C)}$, around 1656 cm^{-1}) to that of the $\alpha CH_2/CH_3$ scissoring mode ($I_{(CH2/CH3)}$, around 1440 cm^{-1}). Using the micro-Raman signal in these lipid modes, the biofuel quality parameters of lipids produced by *C. reinhardtii* under salt stress were calculated. This analysis was performed on an ensemble of ~30 cells and the population average values are shown in **Figure 4.14**. Triolein (18:1C) and microalgal oil (MA Oil) extracted from CSMCRI's *Chlorella variabilis* were used as standards (Raman spectra of MA Oil and Triolein are shown in **Figure 4.15**). Interestingly, the average value of the parameters characterizing biofuel quality (**Figure 4.14**) shows negligible variation for all the culture conditions under study. The average DU obtained for each condition was around 0.6 and the corresponding cetane number (CN) was found to be ~58. The higher heating value (HHV) was found to be around 40 MJ kg^{-1} and the iodine value (IV) was in the range of 60 – 80 mg I_2/ 100 g oil. The fraction of saturated FAs is higher than the unsaturated FAs in all conditions. Interestingly, all the biofuel parameters predicted here show similarity to the standard Triolein, which is a mono-unsaturated 18C long-chain FA containing TAG. These parameters were found to conform with the European standards of biofuel quality (Giakoumis, 2013; Sarakatsanis, 2019) as well as the Indian diesel specifications enumerated by the Ministry of Road Transport and Highways (MoRTH) and the Ministry of Petrol and Natural gas (MoPNG).

Although the lipids produced by *C. reinhardtii* CC-125 under both single-stage and two-stage salt stress conditions were found to yield good biofuel quality, the notable indifference in composition demands an explanation of the impact of salt stress. Ideally, lipid composition can differ for different cells within a culture, and average values do not reveal these hidden heterogeneities in the lipid profile caused by different cell types of a population. Hence, simple averages of cellular response to stressful environments are not suitable parameters to understand the overall population-level response. The significant indifference observed in the population means values of lipid profile upon exposure to salt stress entails an exploration of the response of individual cells in a population for detection of subpopulations with stress response different from the average behavior. The presence of these subpopulations cannot be overlooked, because any stress condition which leads to an enhancement in these subpopulations can cause variations in biofuel quality. The subsequent sections present the heterogeneities in lipid composition.

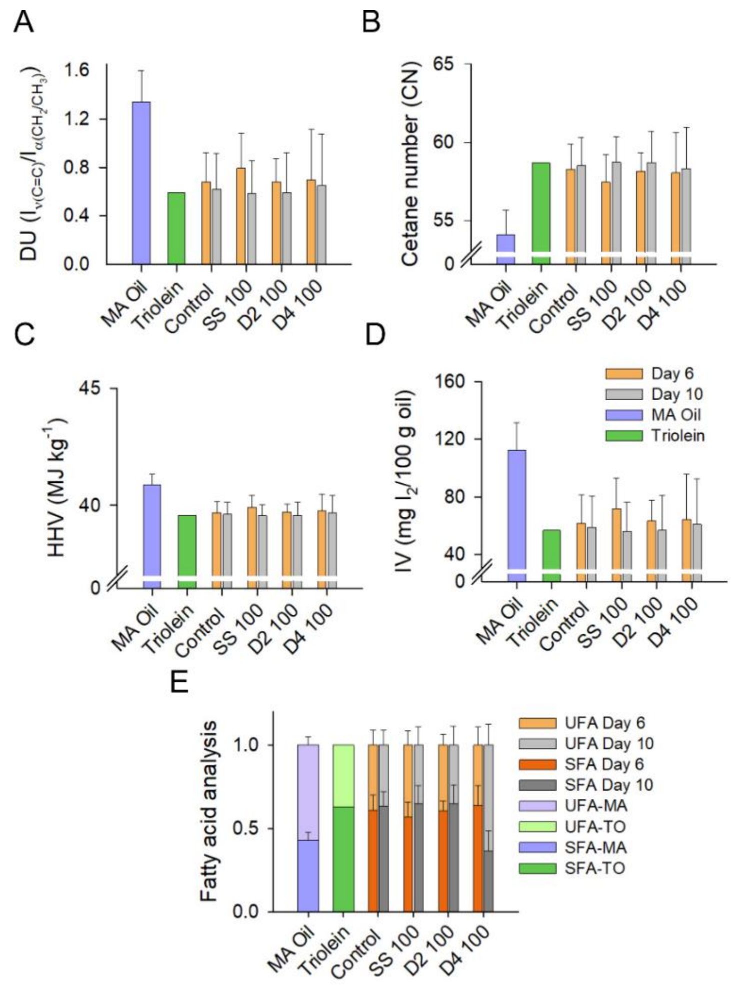

Figure 4.14. Biofuel properties of lipids produced by *C. reinhardtii* under different modes of salt stress.

Degree of unsaturation in **A**., Cetane number in **B.,** Higher heating value in **C.,** and iodine value in **D.** Fraction of saturated (SFA) and unsaturated fatty acid (UFA) in the population in **E**. Microalgal oil (MA Oil, extracted from *Chlorella variabilis* and processed for further use) and Triolein (TO) were used as standards. Values in plots are derived from three independent experiments, with error bars representing the standard deviation.

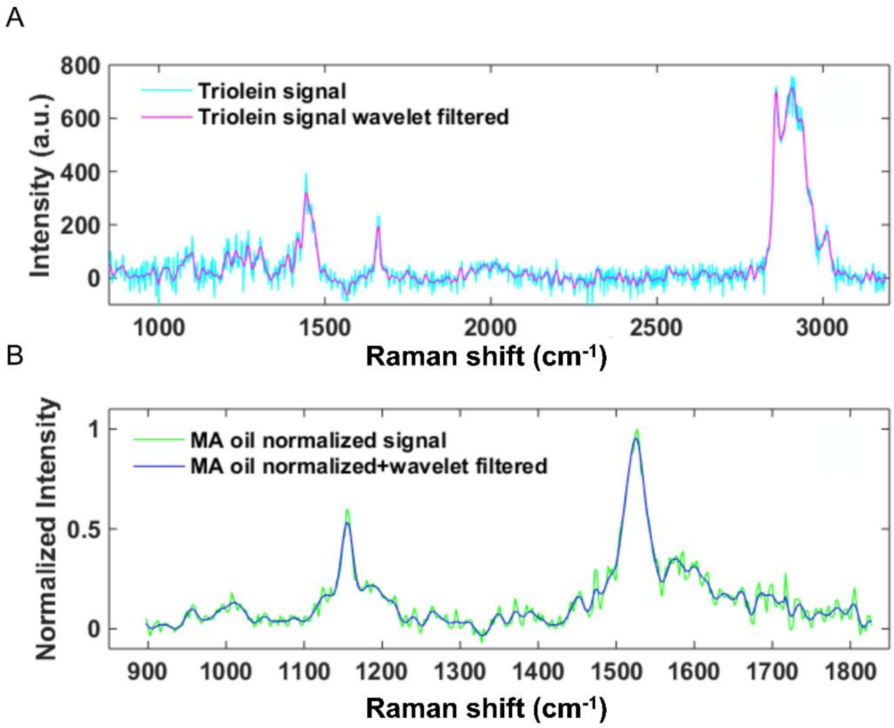

Figure 4.15. Raman spectra of Triolein and microalgal oil after denoising using the DWT approach.

Raman spectra of Triolein (**A**) and microalgal oil (MA Oil) (**B**) are shown after signal decomposition using the same procedure as described in section 4.3.3.

4.4.5.2 Population-scale heterogeneities in fatty acid chain length

Capitalizing on the fact that micro-RS is an efficient tool to carry out high-resolution single-cell studies, we explored lipid composition across individual cells of a single culture. Lipid molecules are characterized by the number of carbon atoms (chain length) present in the FAs and the number of double bonds (degree of unsaturation) defined by the presence of C–C and C=C bonds, respectively. TAGs or triacylglycerol have three FAs esterified to a glycerol molecule, resulting in three C=O bonds and CH_2/CH_3 groups in the FA chain. By analyzing the Raman spectra of several FA methyl esters of different chain lengths, Beattie et al. have correlated the FA chain length to the ratio of the CH_2/CH_3 scissoring mode (I_α) observed around 1440 cm^{-1} and the C=O stretching mode around 1750 cm^{-1} (Beattie et al., 2004). To study this aspect in the present Raman data, normalized histograms were generated for the ratio of peak intensity at 1440 cm^{-1} to 1750 cm^{-1} ($I_{\alpha(CH2/CH3)}$ /$I_{C=O}$, referred to as I_β, **Figure 4.16**) for different culture conditions at Day 6 and Day 10. The histograms could be fitted by the normal distribution function, with some outliers falling at the tails. Broad distribution curves show the presence of cellular diversity, especially for D2 100 D6, D4 100 D6, and D10. We observed that the outliers which are present in the probability distributions of the I_β ratio for the different culture conditions get enhanced in salt stress conditions, demonstrating the presence of substantial cells which respond differently to salt stress in comparison to the average behavior. Overall, the diversity in FA chain length tends to vary under different types of salt stress applications. Further, the mean values obtained from the distribution dictate the average chain length of FA produced in the culture. These values (**Figure 4.16** captions) suggest an overall chain-shortening effect in D4 100, both at D6 and D10. Among the three types of salt stress, the two-stage stress D2 100 is more likely to produce high chain length FAs and D4 100 to produce short-chain FAs throughout the growth of the culture. This analysis shows that salt stress increases heterogeneity in the FA chain length. The heterogeneity further depends on how the salt stress is applied to the growing microalgal culture.

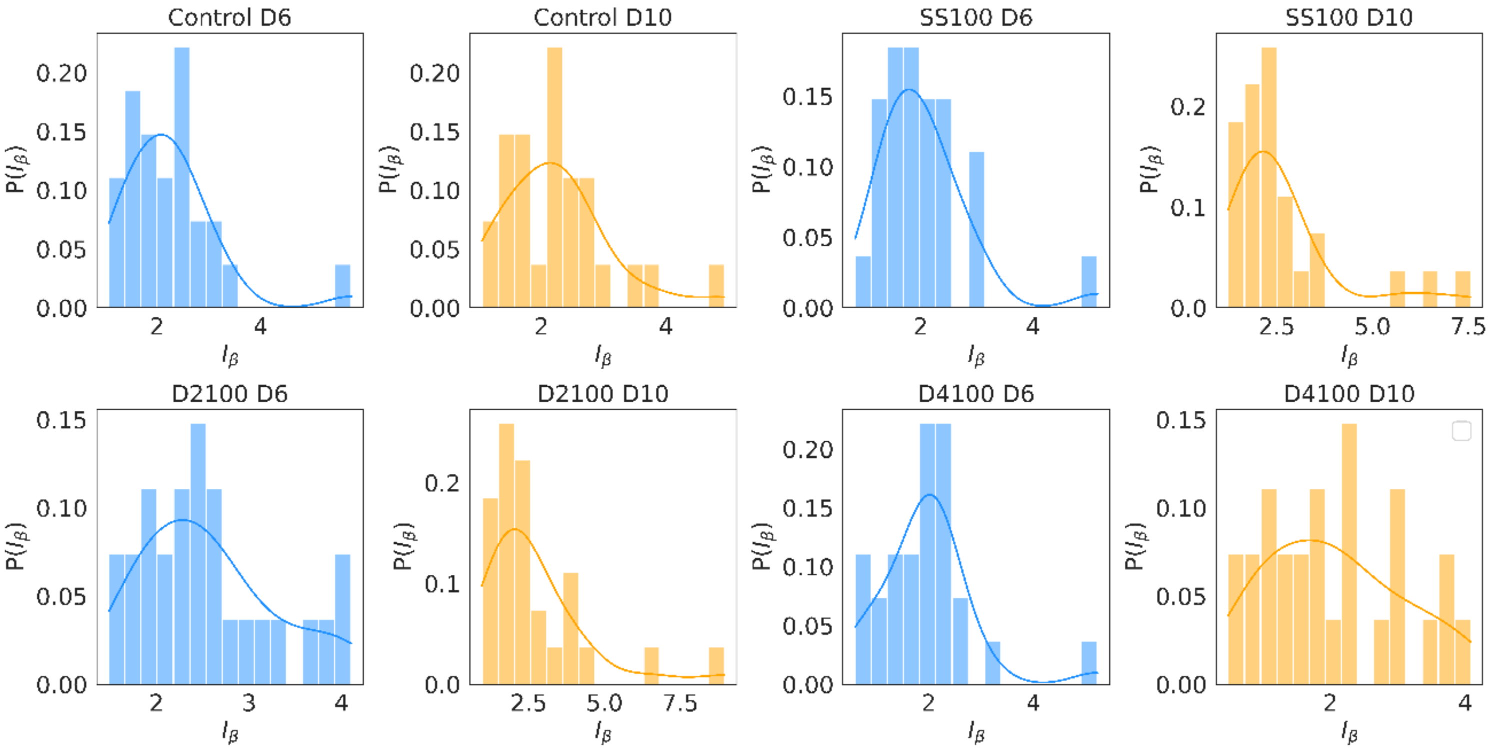

Figure 4.16. Probability distribution of the ratio of $I_{\alpha\ (CH2/CH3)}$ and $I_{C=O}$ (I_β), as a function of incubation time and mode of application of salt stress in *C. reinhardtii*.

Here, P (I_β) represents the probability of occurrence of the peak intensity ratio I_β in the population. The mean values of the I_β ratio obtained from the distribution fit (shown by the solid spline curve, blue for D6 and orange for D10) are 2.24 for Control D6, 2.04 for Control D10, 2.04 for SS 100 D6, 2.47 for SS 100 D10, 2.25 for D2 100 D6, 2.5 for D2 100 D10, 1.95 for D4 100 D6, and 1.73 for D4 100 D10.

4.4.5.3 Effect of salt stress on the degree of unsaturation of lipids

We know now that the unsaturation content of FAs in TAGs is an important criterion that governs biofuel quality. Hence, apart from analyses of heterogeneities in the chain length of FAs, it is necessary to analyze variation in the *C. reinhardtii* population for the unsaturation content of TAGs. The unsaturation content in lipids can be calculated as a ratio of ν(C=C) mode around 1656 cm^{-1}, to the $\alpha(CH_2/CH_3)$ scissoring mode around 1440 cm^{-1}. The Raman intensities at these wavenumbers show a significant peak formation (**Figure 4.17**). A summary statistic of peak centers corresponding to the above modes for cultures grown under different conditions reveals substantial variability in the peak center values of the $\alpha(CH_2/CH_3)$ and ν(C=C) modes (**Figure 4.18**). This variability is characterized by heterogeneity indices (HI) estimated from the OR values. Overall, heterogeneity observed in the $\alpha(CH_2/CH_3)$ scissoring mode is less compared to other peaks studied so far. Most of the cells in the population for all the culture conditions studied have peak center values at 1439 cm^{-1} or 1440 cm^{-1}, except D2 100 at D6 which has a majority of cells with a peak center at 1442 cm^{-1}. For this mode, the HI values at D10 are very high, especially for single-stage SS 100, implying enhanced heterogeneity at the stationary growth phase.

In the case of the ν(C=C) mode distribution, the peak center is mostly observed at 1655 cm^{-1} and 1656 cm^{-1} for the Control culture at D6 and D10 respectively. The HI values are low in Control, but there are outliers. These outliers cannot be neglected, and result in the broadening of the distribution when salt stress is applied, causing variability in the cellular stress response. Under both single and two-stage salt stress, the HI value increases at D10. However, D4 100 has the highest heterogeneity both at D6 as well as at D10, implying the production of lipids with a wide range of unsaturation. Thus, salt stress increases the heterogeneity in the unsaturation content, with maximum HI observed in two-stage, D4 100. This heterogeneity is also enhanced as the culture ages.

We further characterized the distribution of the degree of unsaturation (DU) in lipids under salt stress by carrying out a ratiometric analysis of the Raman peaks at olefinic ν(C=C) stretch which is around 1656 cm^{-1} to the $\alpha(CH_2/CH_3)$ peak around 1440 cm^{-1}, referred to as I_α. Probability density function (PDF), which gives the relative likelihood of the occurrence of the random variable I_{α}, for ~30 *C. reinhardtii* cells for each culture condition was obtained (**Figure 4.19**). We observed symmetrical I_α distributions represented well by the normal distribution for all the D6 cultures except the stress condition D4 100. At D10, the distributions become skewed and asymmetric with larger standard deviations (for D4 100 this is observed both at D6 and D10) and are better described by log-normal function. Overall, a large spread in the I_{α} values illustrating population-scale heterogeneity in lipid DU was observed. Mean I_{α} values calculated from these distributions are found to be around 0.6 in all cases (same as obtained from the analysis described in section 4.4.5.1). The DU distribution for lipids of the D4 100 culture has higher unsaturation degree tails, which is observed to extend to a maximum value of 2, corresponding to 3 C=C bonds (tri unsaturation) irrespective of the culture age (Czamara et al., 2015). On the other hand, SS 100 and D2 100 along with Control show the prevalence of cellular populations with maximum DU of 1.5 – 2.0 towards the stationary phase only, signifying the presence of bi-unsaturated lipids (2 C=C bonds) and tri-unsaturated lipids (3 C=C bonds) at D10, respectively. Thus, different culture conditions have cells that produce lipids with a reasonably wide spectrum of DU values (ranging from mono to tri unsaturation), stressing the fact that the average DU values of around 0.6 (corresponding to mono unsaturation) do not represent the entire population. The inherent heterogeneity in DU present in a population gets more randomized with stress and time. Thus, similar to the heterogeneity observed in the FA chain length, the DU distributions also demonstrate that heterogeneity increases with the age of the culture, and D4 100 shows maximum variability throughout the culture.

Interestingly, a grouping of the degree of unsaturation values using principal component analysis (PCA) based clustering under different growth conditions reveals that two-stage salt stress conditions D4 100 D6 and D10 form a separate cluster, whereas Control D6, SS 100 D6, D2 100 D6, and SS 100 D10 are found to have similar variability (**Figure 4.19C & D**). Control D10 is found to be an outlier. In conclusion, two-stage salt application in D4 100 was observed to have a great impact on the population-scale heterogeneity of the degree of unsaturation.

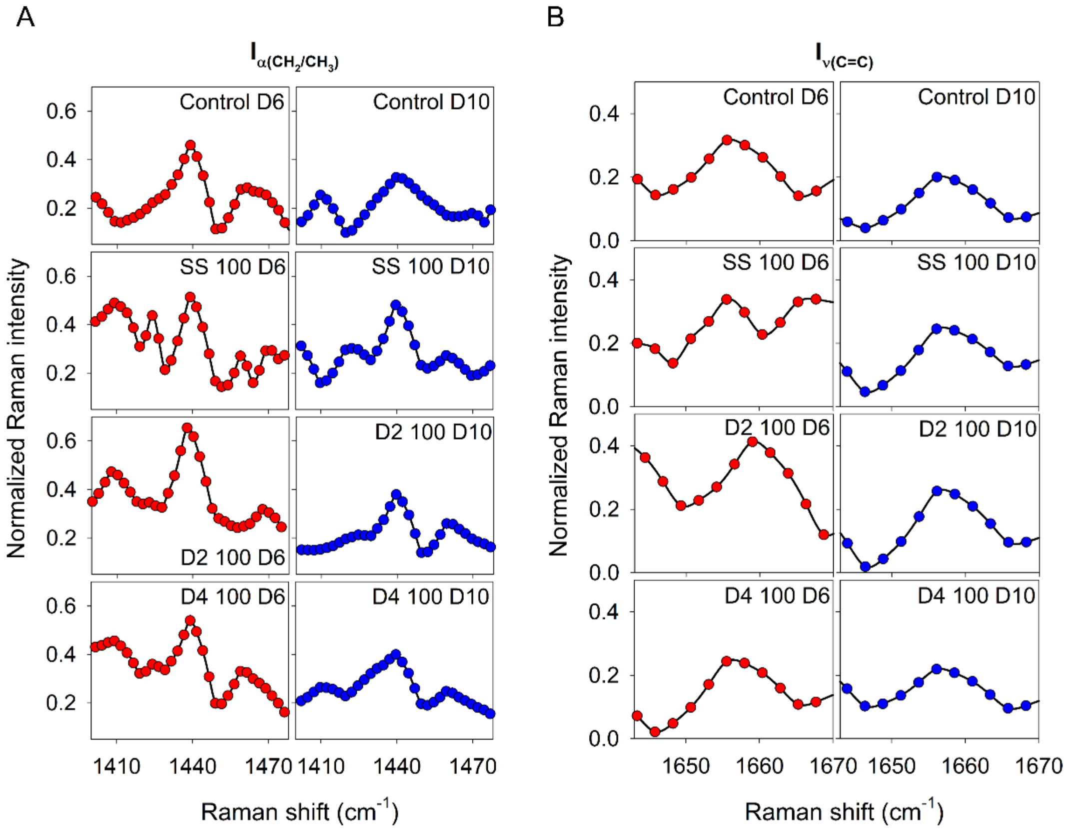

Figure 4.17. Raman intensity at wavenumbers ~1440 and ~1656 cm^{-1} for peaks.

Raman intensity at wavenumbers ~1440 (**A**) and ~1656 cm^{-1} (**B**) for all the culture conditions on day 6 and day 10 shows a prominent peak.

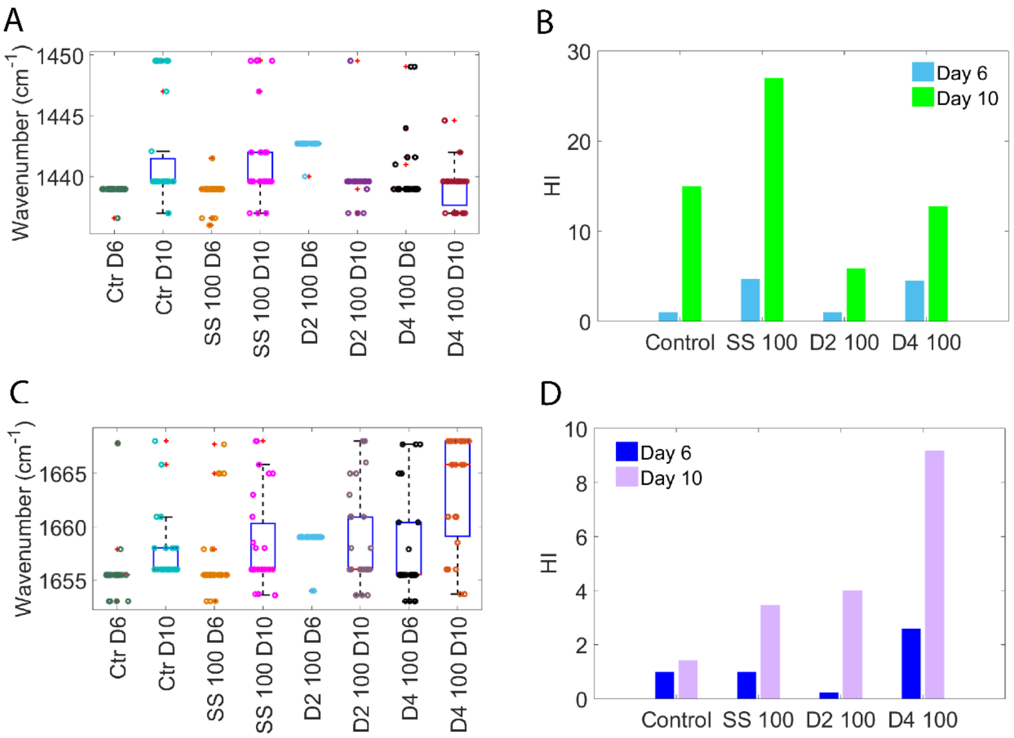

Figure 4.18. Population-scale heterogeneities in the lipid CH_2/CH_3 scissoring mode and C=C stretching mode under salt stress in *C. reinhardtii*.

A and C. Distribution of the α(CH_2/CH_3) scissoring mode and C=C stretching mode respectively for the different salt stress treatments. The central red line in the box plots indicates the median, and the bottom and top edges of the box indicate the 25th and 75th percentiles, respectively. The whiskers extend to the most extreme data points not considered outliers, and the red '+' symbol represents outliers. **B and D.** The heterogeneity index (HI) of the distributions of the α(CH_2/CH_3) scissoring mode and C=C stretching mode respectively at both D6 and D10.

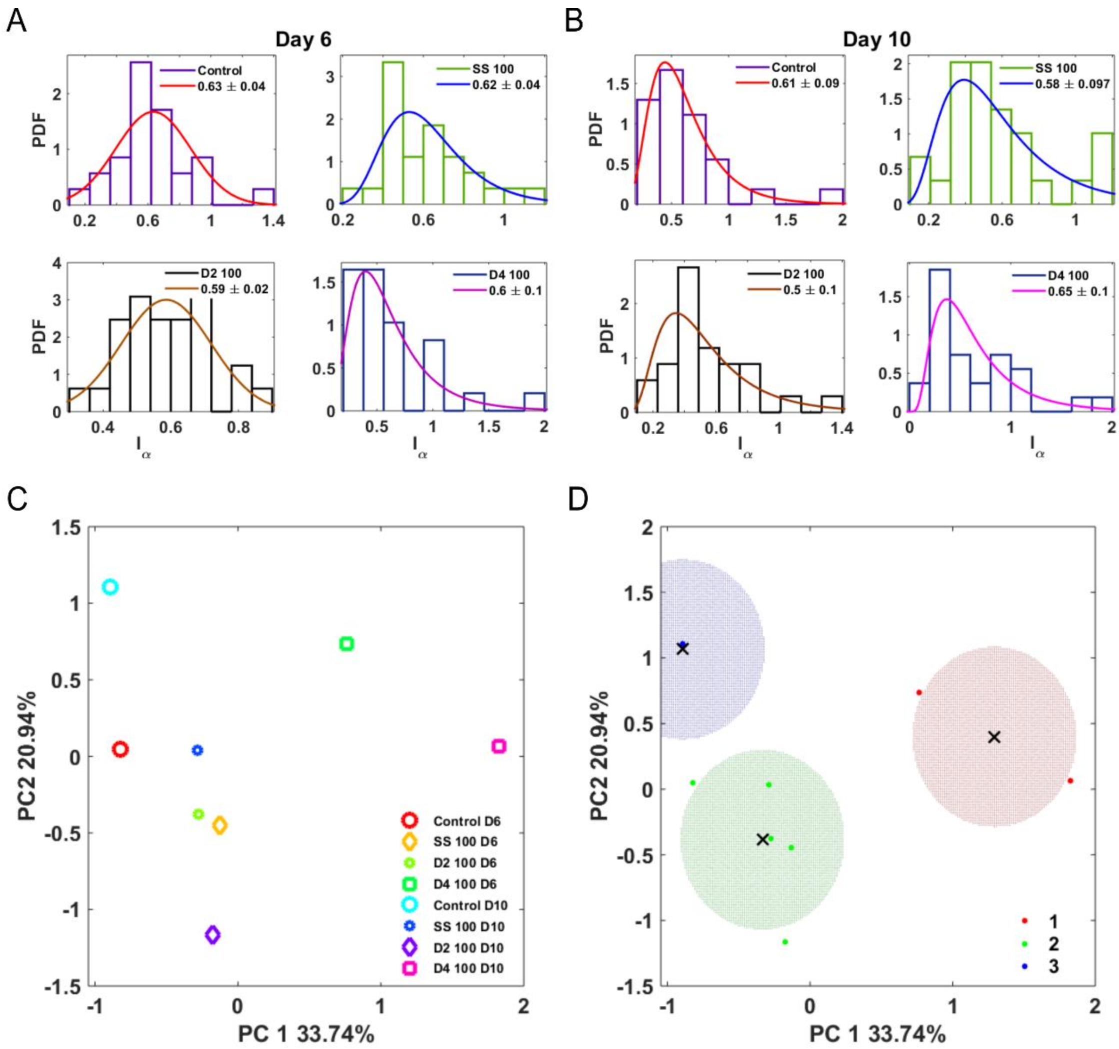

Figure 4.19. Degree of unsaturation of lipids produced by *C. reinhardtii* under different modes of salt stress.

A. Probability density functions (PDF) of DU at D6, mostly fitted well by normal distribution except condition D4 100 (SS 100 histogram is fitted well by both normal and log-normal distribution). **B**. Probability density functions of DU for D10, represented well by a log-normal distribution. The mean of the distribution obtained from the fitted curves is shown in each figure. **C**. A principal component analysis of the degree of unsaturation was studied for different growth conditions. **D**. Cluster analysis depicting three clusters of similar variability between D4 100 D6 and D4 100 D10 (Cluster 1, red), Control D6, SS 100 D6, D2 100 D6, SS 100 D10 and D2 100 D10 (Cluster 2, green), and Control D10 (Cluster 3, blue).

4.5 Discussion

Raman spectroscopy-based techniques such as micro-RS and surface-enhanced Raman scattering (SERS) have become reasonably established methods for label-free, non-invasive, multiplexed detection of cellular biomolecules with good temporal as well as spatial resolution. This study aimed to understand the single-cell heterogeneities in lipid and pigment composition under different modes of salt stress applied to *C. reinhardtii* and standardize the protocol for future use. The method of analyzing Raman spectra presented here aims at extracting spectral information in parallel to maintaining the essential signal integrity and accuracy with a good signal-to-noise ratio using a discrete wavelet transform algorithm (DWT) (**Figures 4.4 & 4.6**). This method, moreover, is more economical compared to high-resolution probes such as Resonance Raman Scattering (RRS), Coherent Anti-Stokes RS (CARS), Stimulated RS (SRS), and Surface-enhanced Raman Spectroscopy (SERS). Single-cell RS has been used as a microalgal cell profiling tool. In a recent study, single-cell lipid profiling was carried out to reveal the degree of unsaturation of lipids for *Scenedesmus quadricauda* grown under nutrient (N_2) deprivation using SERS (Ramya et al., 2017). The present study uncovers cellular-scale heterogeneities in pigment composition, lipid unsaturation, and fatty acid chain length.

When discussing heterogeneities, care should be taken that it is a genuine representation of the cell's metabolite picture. In the present experimental conditions, the focus captures the Raman scattering from only a small fraction (~1/20th) of a *C. reinhardtii* cell, and the presence of a particular biomolecule in the focus is detected with the help of the characteristic fingerprint Raman band of the particular biomolecule. Bright field and fluorescence microscopy images have earlier shown that chlorophyll and lipid droplets are distributed in a large area of the cell for the culture conditions studied (**Figure 2.14**). Lipid droplets have been reported to be distributed in the cytosol (Li-Beisson et al., 2021). Starch, too, is either distributed in the cup-shaped chloroplast stroma or can be found surrounding the pyrenoids (Busi et al., 2014). Thus, the probability of capturing the biomolecules under consideration in the focal point is highly likely. Although absolute quantification is not possible by the method presented here, we show that biomolecular Raman intensities can act as effective biomarkers of stress relative to a control, in addition to enabling a non-invasive detection of biomolecule chemical composition. The major drawback of this high-resolution Raman spectroscopy is the small laser spot size used in this study which does not allow the direct usage of Raman intensities for absolute quantifications. However, several studies have documented the calibration and validation of biomolecular quantification of starch, protein, and lipids using single-cell RS (He et al., 2017). This ability of micro-RS in quantitative measurements is subjected to experimental conditions. Nonetheless, Raman intensities can be used for relative scale measurements. Nile red is a fluorescent dye that selectively stains lipid droplets and allows absolute quantification. Using this approach, it was observed that the lipid content increases in *C. reinhardtii* cells under salt stress (**Figures 2.10 & 4.7**). Also, the distribution becomes more heterogeneous under stress, which is detectable in both Nile red fluorescence and Raman intensity distributions. Salt stress often imposes osmotic imbalance on the cell. Our observations signify that 100 mM NaCl added to the cultures is still below the threshold for such osmotic damage (**Figures 2.4 & 2.15**). Under such circumstances, we determine the inter-play of bio-components, which reveal a disintegrating cellular stasis on day 10 (**Figure 4.8**), especially under salt stress. Thus, Raman spectroscopy is efficient in dictating the cellular level correlation among various bio-components and depending on the experimental conditions can also be used for absolute quantifications.

Raman spectroscopy of chlorophylls and carotenoids

Pigment analysis by biochemical extraction method is purely quantitative rather than qualitative. These are labor-intensive and do not give any idea of the presence of cells in the population which behave significantly different compared to the average. Moreover, since no composition-dependent estimate is available, the best time to harvest carotenoids is difficult to determine since the carotenoid content in D6 and D10 is similar. There is no information obtained from the spectrophotometric estimation on the type of carotenoids produced under different growth conditions. To overcome these drawbacks, single-cell micro-Raman spectroscopic studies were carried out without extracting the pigments.

Carotenoids have many conformational states, as revealed by femtosecond spectroscopy (Liguori et al., 2017). These conformational changes are triggered by conformational switching in the LHCs from the highly fluorescent light-harvesting state to the quenched, dissipative state (Liguori et al., 2017). In the quenched state of LHCs, carotenoids are observed to have twisted conformations. It has been observed by Liguori et al. that the orientation of lutein within LHCs is functionally important for the regulation of light-harvesting efficiency, and photo protection to prevent photo oxidative stress and damage to PSI and PSII. Several studies have shown that transition to the dissipative state is triggered by the conformational changes in the antenna complexes of LHCs, leading to the detection of several conformational changes in carotenoids (Son et al., 2020; Pascal et al., 2005; Yan et al., 2007). Different conditions modify carotenoid conformations, resulting in changes in relative orientation between chlorophyll and carotenoids in the antenna complexes, which affect the sensitive electronic interactions between the two molecules. Femtosecond stimulated Raman spectroscopy has clearly shown the presence of two *β*-carotene conformations involved in the chlorophyll quenching mechanism for photo protection (Hontani et al., 2018). The intensity of carotenoid Raman bands has also been observed to increase due to an out-of-plane distortion when bound to microbial reaction centers (Lutz et al., 1987). The xanthophyll cycle and lutein have been demonstrated to play an important role in the protection of PSII against photo oxidative stress (Jahns and Holzwarth, 2012). Salinity stress leads to ROS production, and excess energy dissipation with ROS deactivation by the quenched state of the LHCs thus involving variable carotenoid conformations. Hence, apart from the changes in carotenoid content in different cells, different conformational states can occur, which can reflect in the intensity of carotenoid Raman modes, which would be interesting to analyze. Li *et al.* have observed that the C=C stretching mode (car-i) of lutein is at 1532 cm^{-1}, whereas that of zeaxanthin occurs at 1528 cm^{-1} (Li et al., 2020). Since the position of the C=C stretching mode (car-i) depends on the length of conjugation, lutein, having 10 conjugated C=C bonds has a higher C=C stretching mode peak center than zeaxanthin, which has a conjugation length of 11. They observed that protein-bound lutein and zeaxanthin have an unchanged car-i peak position. Thus, the shifting of car-i mode peak center to higher wave numbers in *C. reinhardtii* cultures with age and salinity stress observed presently could be purely due to a contribution from different types of carotenoids such as lutein, zeaxanthin, or *β*-carotene, and maybe not due to changes introduced due to carotenoid binding with the other proteins in LHC. This shift also signifies the enhancement of the content of lutein and zeaxanthin in the cells, since *β*-carotene has the car-i mode peak center at 1520 cm^{-1}. Therefore in the present study, compositional heterogeneities revealed the increase in the presence of carotenoids other than β-carotene, i.e., lutein and zeaxanthin, in the cultures grown under salt stress, and with increasing age of the culture.

Chlorophyll fluorescence studies on the microalga *Scenedesmus obliquus* have shown that salinity stress affects photosynthetic efficiency by damaging the PSII reaction center which leads to loss of electron transfer and light-harvesting efficiency (Ji et al., 2018). Several studies are showing a decrease in chlorophyll content in microalgal cells under salinity stress (Demetriou et al., 2007; Kaňa and Govindjee, 2016). Excess intracellular sodium ions can affect K^+-Na^+ ion balance across thylakoid membranes, dysregulating the production of ATP by ion channels, thus inhibiting the photosynthetic light-harvesting process. Increased salinity increases intracellular ROS, which results in increased content of carotenoids, leading to more quenched stats of the LHCs. Thus, increased salt content has multiple inhibitory effects on photosynthesis. Micro-Raman spectral analyses shown here indicate a decrease in chl-iii mode intensity (**Figure 4.11**) in *C. reinhardtii* cells with age and salinity stress, which is corroborated by single-cell population fraction measurements by microscopy. It is possible that apart from affecting the chlorophyll content, salinity stress also produces conformational or structural changes in chlorophylls in *C. reinhardtii* cells. Chlorophyll fluorescence studies on the green microalgae *Scenedesmus obliquus* have revealed that salinity stress changes the photosystem structure by expanding the functional size of the antenna complex and reducing the density of active PSII reaction centers [30]. Various chlorophyll fluorescence studies reveal structural changes in LHCs under abiotic stresses (Murchie and Lawson, 2013; Patil et al., 2017). Thus, the changes observed in the chlorophyll Raman mode intensities could also arise due to salinity stress-induced changes in the LHC structure where autophagy, a well-known phenomenon that causes the degradation of chloroplasts and chlorophylls, can also play an important role under such stressful conditions (Gorelova et al., 2019).

Raman spectroscopy of lipids

Most uniquely, this study used the Raman spectral information of the lipid molecules, and the biofuel quality parameters were determined for the lipids produced under salt stress by *C. reinhardtii*. We found that salt stress leads to lipid production of good biofuel quality in *C. reinhardtii* (**Figure 4.14**). The higher heating value (HHV) and iodine value (IV) were found to be around 40 MJ kg^{-1} and 60 – 80 mg I_2/ 100 g oil, respectively. These values intend to make the extracted oil yield high combustion energy (Calixto et al., 2018) and hence follow both, the European as well as Indian diesel specifications. Moreover, the average degree of unsaturation values (0.6) observed shows the predominance of mono-unsaturated TAGs making the oil oxidative stable (Calixto et al., 2018; Giakoumis, 2013). These properties are observed to be well aligned with the standard Triolein (18:1). This analysis, the first of its kind to our best knowledge, renders the suitability of Raman spectroscopy to utilize for efficient biofuel quality determination. However, all the conditions under study revealed an insignificant difference in these properties among themselves. This behavior was intriguing enough to look for single-cell spectral information.

Ratiometric intensity probability distribution analysis for $I_{\alpha(CH2/CH3)}$ /$I_{C=O}$ (**Figure 4.16**) suggests that shorter chain length FAs are produced more during two-stage salt stress condition D4 100, both during the stationary growth phase and exponential growth phase. A possible reason for chain shortening with age and salt stress could be the activation of the β-oxidation pathway under stress (Kong et al., 2018), where enzymatic degradation of lipids takes place to release energy in the form of ATP. It can also be due to autophagy, a hint of which is evident in the correlation analysis as well from the negative carotenoids and starch/lipids correlation (Davey et al., 2014). Autophagy is a catabolic process and is activated to counterbalance the effect of stress on the cell by recycling the damaged material to maintain the cell’s homeostasis (Couso et al., 2017). Note that not all the cells had the same response to the environment, and some decided to drift and form a subpopulation exhibiting different behavior, giving rise to heterogeneities.

The major question arises, what is the biological implication of this heterogeneity? It has been well-documented that heterogeneous behavior is often induced when microbial cultures face environmental stress (Martins and Locke, 2015; Lidstrom and Konopka, 2010). Stress can also include a shortage of nutrient availability as the culture attains its stationary phase. Under such a stressful condition, subpopulations present inside one main population account for one of the population-level strategies for adaptation and evolution. In this case, the subpopulation of cells exhibiting Raman peak at around 1086 cm^{-1} starts to appear by day 6 and increases in size by day 10, under salt stress. This indicates the development of a gradual adaptive response of cells towards salt stress. The heterogeneity index (HI) further elaborates on the multiple subpopulations present. It is more prominent in the case of lipid unsaturation on day 10 when multiples of subpopulation increase (**Figure 4.18**), also evident by the tails of probability distribution curves (**Figure 4.19**), characterized as higher unsaturation content. This increase in subpopulation size on day 10 exhibiting bi-tri unsaturation directs at some adaptation strategy of the population as the culture progresses towards death. Note, that this behavioral response of the population could not be detected in average measurements (average unsaturation content measured was mono- under all the culture conditions, **Figure 4.16**). Finally, D4 100 shows an equally widespread distribution on both day 6 and day 10 especially in the case of olefinic ν(C=C) stretch at around 1656 cm^{-1} and stands out as a separate cluster (**Figure 4.19**). An overall increased heterogeneity in D4 100 shows that this strategy of salt stress application imposes more variable choices on the population. It allows several groups to undergo different transcriptome and proteome development to explore the best possible mechanism of fitness (Cross and Umen, 2015). This makes D4 100 way different than its other two-stage counterpart, D2 100. This way, Raman spectroscopy-oriented heterogeneity studies allow us to understand the possible response of individual cells in a population and their coherent effort in population survival. Such variability within a single culture could be an important technical concern during large-scale growth for industrial-scale biofuel production. Although synchronization offers homogeneity in the culture, it too can develop heterogeneities with longer incubation time (Tanay et al., 2018), similar to what is observed in the isogenic culture of *Nannochloropsis oceanica* under nitrogen depletion (Wang et al., 2014).

To summarize, micro-RS efficiently reveals single-cell heterogeneities which increase under salt stress and at the stationary phase of growth. The main highlight of the study is the production of varying lipid and carotenoid composition in *C. reinhardtii* under salt stress, which further changes with the mode of cultivation (**Figure 4.20**). This study as per our knowledge serves to be the first of its kind to deliver such a detailed insight into the microalgal lipid and pigment heterogeneities as a function of salt stress and growth.

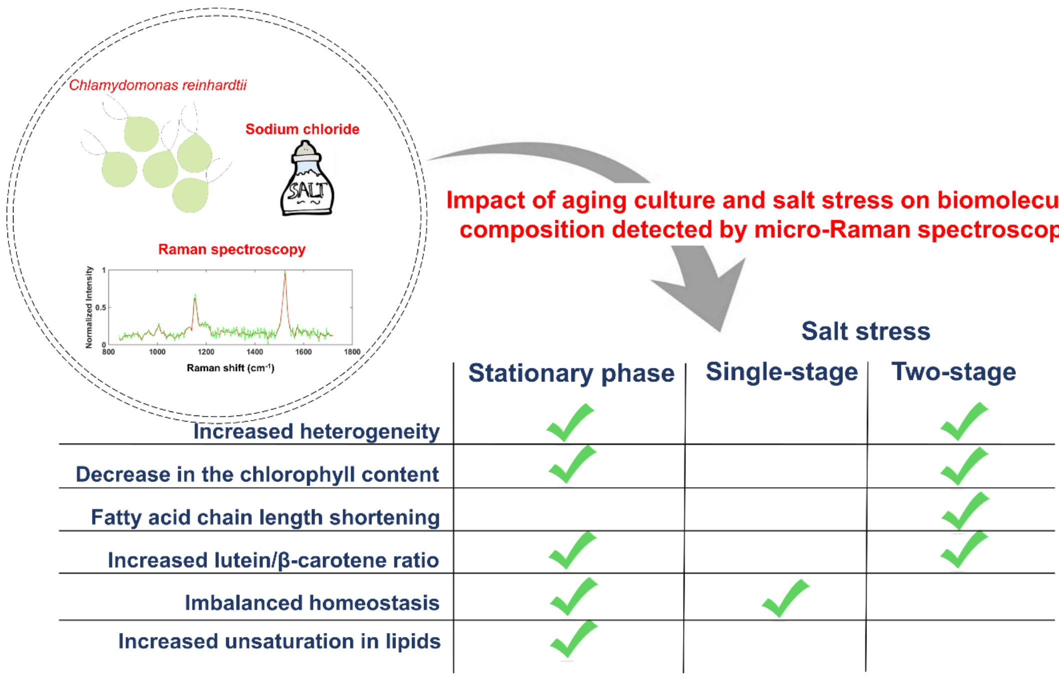

Figure 4.20. The overall impact of the aging culture of *C. reinhardtii* and salt stress on lipid profile, carotenoid composition, and chlorophyll content detected by micro-Raman spectroscopy

4.6 Conclusion

In this study, the versatility of micro-Raman spectroscopy is exploited for non-invasive single-cell metabolic profiling of LHC pigments and lipid molecules produced under single-stage and two-stage salt stress in *Chlamydomonas reinhardtii* CC-125. Raman spectroscopy is identified as a powerful tool for potential quantitative estimates of chlorophylls and carotenoids as well as analyzing the photosynthetic efficiency of cells. With the help of heterogeneity indices obtained for the FA chain length and unsaturation content in the TAGs, this micro-RS study detects the overlooked presence of sub-populations in a culture, which is never acknowledged in the mass measurements. Unicellular microalgal cells when growing as a population adopt strategies to combat stress as a population. Distributing the workload and trying different survival methods is one such strategy that gives rise to single-cell heterogeneities and possibly provides a means of evolution in the long run. This variability forms an inherent property of a population that was observed to fluctuate under salinity stress in *C. reinhardtii*.

The present knowledge encourages more such single-cell studies in microalgal research to understand the interplay of the abiotic factors and the cellular response in an exploratory manner. Lastly, we conclude that heterogeneity could serve as a potential bottleneck for good lipid and carotenoid productivity of uniform quality in large-scale cultures, a factor that needs serious attention. Micro-Raman spectroscopy is established to be a very efficient tool for non-invasive, high throughput, and high-resolution multivariate analysis necessary for high throughput optimizations of culture conditions. Overall, micro-Raman spectroscopy revealed important features of pigment production and lipid composition in microalgae, which can be potentially useful for optimizing conditions for increased industrial-scale productivity.

4.7 References

Abomohra, A.E.F., A.H. El-Naggar, S.O. Alaswad, M. Elsayed, M. Li, and W. Li. 2020. Enhancement of biodiesel yield from a halophilic green microalga isolated under extreme hypersaline conditions through stepwise salinity adaptation strategy. *Bioresour. Technol.* 310:123462. doi:10.1016/j.biortech.2020.123462.

Ali, H.E.A., E.A. El-fayoumy, W.E. Rasmy, R.M. Soliman, and M.A. Abdullah. 2021. Two-stage cultivation of *Chlorella vulgaris* using light and salt stress conditions for simultaneous production of lipid, carotenoids, and antioxidants. *J. Appl. Phycol.* 33:227–239. doi:10.1007/s10811-020-02308-9.

Altschuler, S.J., and L.F. Wu. 2010. Cellular Heterogeneity: Do Differences Make a Difference? *Cell*. 141:559–563. doi:10.1016/j.cell.2010.04.033.

Aziz, M.M.A., K.A. Kassim, Z. Shokravi, F.M. Jakarni, H.Y. Lieu, N. Zaini, L.S. Tan, S. Islam, and H. Shokravi. 2020. Two-stage cultivation strategy for simultaneous increases in growth rate and lipid content of microalgae: A review. *Renew. Sustain. Energy Rev.* 119:109621. doi:10.1016/j.rser.2019.109621.

Baladehi, M.H., M. Hekmatara, Y. He, Y. Bhaskar, Z. Wang, L. Liu, Y. Ji, and J. Xu. 2021. Culture-free identification and metabolic profiling of microalgal single cells via ensemble learning of ramanomes. *Anal. Chem.* doi:10.1021/acs.analchem.1c01015.

Beattie, J.R., S.E.J. Bell, and B.W. Moss. 2004. A critical evaluation of Raman spectroscopy for the analysis of lipids: Fatty acid methyl esters. *Lipids*. 39:407–419. doi:10.1007/s11745-004-1245-z.

Bhattacharya, S., R. Maurya, S. Kumar, and T. Ghosh. 2016. Solar driven mass cultivation and the extraction of lipids from *Chlorella variabilis* : A case study. *ALGAL*. 14:137–142. doi:10.1016/j.algal.2016.01.009.

Busi, M. V., J. Barchiesi, M. Martín, and D.F. Gomez-Casati. 2014. Starch metabolism in green algae. *Starch/Staerke*. 66:28–40. doi:10.1002/star.201200211.

Calixto, C.D., J.K. da Silva Santana, V.P. Tibúrcio, L. de F.B.L. de Pontes, C.F. da Costa Sassi, M.M. da Conceição, and R. Sassi. 2018. Productivity and fuel quality parameters of lipids obtained from 12 species of microalgae from the northeastern region of Brazil. *Renew. Energy*. 115:1144–1152. doi:10.1016/j.renene.2017.09.029.

Challagulla, V., S. Nayar, K. Walsh, and L. Fabbro. 2016. Critical Reviews in Biotechnology Advances in techniques for assessment of microalgal lipids. 8551:0–13. doi:10.1080/07388551.2016.1206058.

Cheng, D., and Q. He. 2014. Assessment of environmental stresses for enhanced microalgal biofuel production – an overview. 2:1–8. doi:10.3389/fenrg.2014.00026.

Chiu, L. Da, S.H. Ho, R. Shimada, N.Q. Ren, and T. Ozawa. 2017. Rapid in vivo lipid/carbohydrate quantification of single microalgal cell by Raman spectral imaging to reveal salinity-induced starch-to-lipid shift. *Biotechnol. Biofuels*. 10:1–9. doi:10.1186/s13068-016-0691-y.

Couso, I., M.E. Pérez-Pérez, E. Martínez-Force, H.-S. Kim, Y. He, J.G. Umen, J.L. Crespo, and P. Bozhkov. 2017. Autophagic flux is required for the synthesis of triacylglycerols and ribosomal protein turnover in *Chlamydomonas*. *J. Exp. Bot.* doi:10.1093/jxb/erx372.

Cross, F.R., and J.G. Umen. 2015. The *Chlamydomonas* cell cycle. *Plant J.* 82:370–392. doi:10.1111/tpj.12795.

Czamara, K., K. Majzner, M.Z. Pacia, K. Kochan, A. Kaczor, and M. Baranska. 2015. Raman spectroscopy of lipids: A review. *J. Raman Spectrosc.* 46:4–20. doi:10.1002/jrs.4607.

Davey, M.P., I. Horst, G.H. Duong, E. V. Tomsett, A.C.P. Litvinenko, C.J. Howe, and A.G. Smith. 2014. Triacylglyceride Production and Autophagous Responses in *Chlamydomonas reinhardtii* Depend on Resource Allocation and Carbon Source. *Eukaryot. Cell*. 13:392–400. doi:10.1128/EC.00178-13.

Dębowski, M., M. Zieliński, J. Kazimierowicz, N. Kujawska, and S. Talbierz. 2020. Microalgae cultivation technologies as an opportunity for bioenergetic system development—advantages and limitations. *Sustain.* 12:1–37. doi:10.3390/su12239980.

Dekker, J.P., and E.J. Boekema. 2005. Supramolecular organization of thylakoid membrane proteins in green plants. *Biochim. Biophys. Acta*. 1706:12–39. doi:10.1016/j.bbabio.2004.09.009.

Demetriou, G., C. Neonaki, E. Navakoudis, and K. Kotzabasis. 2007. Salt stress impact on the molecular structure and function of the photosynthetic apparatus—The protective role of polyamines. *Biochim. Biophys. Acta - Bioenerg.* 1767:272–280. doi:https://doi.org/10.1016/j.bbabio.2007.02.020.

Demirbas, A., and M.F. Demirbas. 2011. Importance of algae oil as a source of biodiesel. *Energy Convers. Manag.* 52:163–170. doi:10.1016/j.enconman.2010.06.055.

Drop, B., M. Webber-Birungi, S.K.N. Yadav, A. Filipowicz-Szymanska, F. Fusetti, E.J. Boekema, and R. Croce. 2014. Light-harvesting complex II (LHCII) and its supramolecular organization in *Chlamydomonas reinhardtii*. *Biochim. Biophys. Acta*. 1837:63–72. doi:10.1016/j.bbabio.2013.07.012.

Elizabeth, C.E., P.K. Lakshmi, S. Meenakshi, S. Vaidyanathan, S. Srisudha, and M.B. Mary. 2020. Spectrochimica Acta Part A : Molecular and Biomolecular Spectroscopy Biomolecular transitions and lipid accumulation in green microalgae monitored by FTIR and Raman analysis. *Spectrochim. Acta Part A Mol. Biomol. Spectrosc.* 224:117382. doi:10.1016/j.saa.2019.117382.

Elowitz, M.B., A.J. Levine, E.D. Siggia, and P.S. Swain. 2002. Stochastic Gene Expression in a Single Cell. *Science (80-.).* 297:1183–1186. doi:10.1126/science.1070919.

Ghosh, P.K., S.C.. Mishra, S. Maiti, C. Paliwal, S.K. Mishra, T. Ghosh, P. Patel, and J.N. Bharadia. 2015. Solar driven solvent extractor and process for extraction of microalgal lipids using the same field. US 2015:1–5.

Giakoumis, E.G. 2013. A statistical investigation of biodiesel physical and chemical properties , and their correlation with the degree of unsaturation. *Renew. Energy*. 50:858–878. doi:10.1016/j.renene.2012.07.040.

Gorelova, O., O. Baulina, T. Ismagulova, K. Kokabi, E. Lobakova, I. Selyakh, L. Semenova, O. Chivkunova, O. Karpova, P. Scherbakov, I. Khozin-Goldberg, and A. Solovchenko. 2019. Stress-induced changes in the ultrastructure of the photosynthetic apparatus of green microalgae. *Protoplasma*. 256:261–277. doi:10.1007/s00709-018-1294-1.

He, Y., P. Zhang, S. Huang, T. Wang, Y. Ji, and J. Xu. 2017. Label-free, simultaneous quantification of starch, protein and triacylglycerol in single microalgal cells. *Biotechnol Biofuels*. 10:1–18. doi:10.1186/s13068-017-0967-x.

Hontani, Y., M. Kloz, T. Polívka, M.K. Shukla, R. Sobotka, and J.T.M. Kennis. 2018. Molecular Origin of Photoprotection in Cyanobacteria Probed by Watermarked Femtosecond Stimulated Raman Spectroscopy. *J. Phys. Chem. Lett.* 9:1788–1792. doi:10.1021/acs.jpclett.8b00663.

Huang, Y.Y., C.M. Beal, W.W. Cai, R.S. Ruoff, and E.M. Terentjev. Micro-Raman Spectroscopy of Algae : Composition Analysis and Fluorescence Background Behavior. doi:10.1002/bit.22617.

Huang, Y.Y., C.M. Beal, W.W. Cai, R.S. Ruoff, and E.M. Terentjev. 2010. Micro-Raman spectroscopy of algae: Composition analysis and fluorescence background behavior. *Biotechnol. Bioeng.* 105:889–898. doi:10.1002/bit.22617.

Jaeger, D., C. Pilger, H. Hachmeister, E. Oberländer, R. Wördenweber, J. Wichmann, J.H. Mussgnug, T. Huser, and O. Kruse. 2016. Label-free in vivo analysis of intracellular lipid droplets in the oleaginous microalga *Monoraphidium neglectum* by coherent Raman scattering microscopy. *Sci. Rep.* 6:2–10. doi:10.1038/srep35340.

Jahns, P., and A.R. Holzwarth. 2012. The role of the xanthophyll cycle and of lutein in photoprotection of photosystem II. *Biochim. Biophys. Acta*. 1817:182–193. doi:10.1016/j.bbabio.2011.04.012.

Jehlička, J., H.G.M.M. Edwards, K. Osterrothová, J. Novotná, L. Nedbalová, J.J. Kopecký, I. Němec, and A. Oren. 2014. Potential and limits of Raman spectroscopy for carotenoid detection in microorganisms: Implications for astrobiology. *Philos. Trans. R. Soc. A Math. Phys. Eng. Sci.* 372. doi:10.1098/rsta.2014.0199.

Ji, X., J. Cheng, D. Gong, X. Zhao, Y. Qi, Y. Su, and W. Ma. 2018. The effect of NaCl stress on photosynthetic efficiency and lipid production in freshwater microalga-*Scenedesmus obliquus* XJ002. *Sci. Total Environ.* 633:593–599.

Kaňa, R., and Govindjee. 2016. Role of Ions in the Regulation of Light-Harvesting. *Front. Plant Sci.* 7:1849. doi:10.3389/fpls.2016.01849.

Kong, F., I.T. Romero, Y. Li-beisson, and J. Warakanont. 2018. Lipid catabolism in microalgae. doi:10.1111/nph.15047.

Kose, A., and S.S. Oncel. 2017. Algae as a promising resource for biofuel industry: facts and challenges. *Int. J. Energy Res.* 41:924–951. doi:10.1002/er.3699.

Li-Beisson, Y., F. Kong, P. Wang, Y. Lee, and B.H. Kang. 2021. The disassembly of lipid droplets in *Chlamydomonas*. *New Phytol.* 231:1359–1364. doi:10.1111/nph.17505.

Li, B., E.W. George, G.T. Rognon, A. Gorusupudi, A. Ranganathan, F.-Y. Chang, L. Shi, J.M. Frederick, and P.S. Bernstein. 2020. Imaging lutein and zeaxanthin in the human retina with confocal resonance Raman microscopy. *Proc. Natl. Acad. Sci. U. S. A.* 117:12352–12358. doi:10.1073/pnas.1922793117.

Lidstrom, M.E., and M.C. Konopka. 2010. The role of physiological heterogeneity in microbial population behavior. *Nat. Chem. Biol.* 6:705–712. doi:10.1038/nchembio.436.

Liguori, N., P. Xu, I.H.M. Van Stokkum, B. Van Oort, Y. Lu, D. Karcher, R. Bock, and R. Croce. 2017. Different carotenoid conformations have distinct functions in light-harvesting regulation in plants. *Nat. Commun.* 8:1–9. doi:10.1038/s41467-017-02239-z.

Liu, Z., H. Yan, K. Wang, T. Kuang, J. Zhang, L. Gui, X. An, and W. Chang. 2004. Crystal structure of spinach major light-harvesting complex at 2.72 A resolution. *Nature*. 428:287–292. doi:10.1038/nature02373.

Lutz, M., W. Szponarski, G. Berger, B. Robert, and J.-M. Neumann. 1987. The stereoisomerism of bacterial, reaction-center-bound carotenoids revisited: An electronic absorption, resonance Raman and 1H-NMR study. *Biochim. Biophys. Acta - Bioenerg.* 894:423–433. doi:https://doi.org/10.1016/0005-2728(87)90121-6.

Martins, B.M.C., and J.C.W. Locke. 2015. Microbial individuality: how single-cell heterogeneity enables population level strategies. *Curr. Opin. Microbiol.* 24:104–112. doi:10.1016/j.mib.2015.01.003.

Mehta, M., R. Naffa, W. Zhang, N.M. Schreurs, M. Waterland, S. Cooper, and G. Holmes. 2021. Validity and reliability of Raman spectroscopy for carotenoid assessment in cattle skin. *Biochem. Biophys. Reports*. 27:101036. doi:10.1016/j.bbrep.2021.101036.

Moser, B.R. 2009. Biodiesel production, properties, and feedstocks. *Vitr. Cell. Dev. Biol. - Plant*. 45:229–266. doi:10.1007/s11627-009-9204-z.

Murchie, E.H., and T. Lawson. 2013. Chlorophyll fluorescence analysis: a guide to good practice and understanding some new applications. *J. Exp. Bot.* 64:3983–3998. doi:10.1093/jxb/ert208.

Natali, A., and R. Croce. 2015. Characterization of the major light-harvesting complexes (LHCBM) of the green alga *Chlamydomonas reinhardtii*. *PLoS One*. 10. doi:10.1371/journal.pone.0119211.

Nekvapil, F., A. Bunge, L. Barbu Tudoran, and S. Cintă Pinzaru. 2021. Single-cell Raman micro-spectroscopy for tracking of carotenoids in Cyanobacteria exposed to Mn and Zn doped ferrite nanoparticles. *Spectrochim. Acta - Part A Mol. Biomol. Spectrosc.* 254. doi:10.1016/j.saa.2021.119607.

De Oliveira, V.E., M.A.C.N. Miranda, M.C.S. Soares, H.G.M. Edwards, and L.F.C. De Oliveira. 2015. Study of carotenoids in Cyanobacteria by Raman spectroscopy. *Spectrochim. Acta - Part A Mol. Biomol. Spectrosc.* 150:373–380. doi:10.1016/j.saa.2015.05.044.

Osterrothová, K., A. Culka, K. Němečková, D. Kaftan, L. Nedbalová, L. Procházková, and J. Jehlička. 2019. Analyzing carotenoids of snow algae by Raman microspectroscopy and high-performance liquid chromatography. *Spectrochim. Acta - Part A Mol. Biomol. Spectrosc.* 212:262–271. doi:10.1016/j.saa.2019.01.013.

Paliwal, C., M. Mitra, K. Bhayani, S.V.V. Bharadwaj, T. Ghosh, S. Dubey, and S. Mishra. 2017. Abiotic stresses as tools for metabolites in microalgae. *Bioresour. Technol.* 244:1216–1226. doi:10.1016/j.biortech.2017.05.058.

Pascal, A.A., Z. Liu, K. Broess, B. van Oort, H. van Amerongen, C. Wang, P. Horton, B. Robert, W. Chang, and A. Ruban. 2005. Molecular basis of photoprotection and control of photosynthetic light-harvesting. *Nature*. 436:134–137. doi:10.1038/nature03795.

Patil, S., R. Pandit, and A. Lali. 2017. Photosynthetic acclimation of *Chlorella saccharophila* to heat stress. *Phycol. Res.* 65:160–165. doi:https://doi.org/10.1111/pre.12171.

Ramya, A.N., P.S. Ambily, B.S. Sujitha, M. Arumugam, and K. Kumar. 2017. Single cell lipid profiling of *Scenedesmus quadricauda* CASA-CC202 under nitrogen starved condition by surface enhanced Raman scattering (SERS) fingerprinting. 25:200–206. doi:10.1016/j.algal.2017.05.011.

Rygula, A., K. Majzner, K.M. Marzec, A. Kaczor, and M. Pilarczyk. 2013. Raman spectroscopy of proteins : a review. 1061–1076. doi:10.1002/jrs.4335.

Sarakatsanis, C.K. 2019. A Comparative Assessment of Biodiesel Cetane Acid Composition. 1–30. doi:10.3390/en12030422.

Son, M., A. Pinnola, S.C. Gordon, R. Bassi, and G.S. Schlau-Cohen. 2020. Observation of dissipative chlorophyll-to-carotenoid energy transfer in light-harvesting complex II in membrane nanodiscs. *Nat. Commun.* 11:1295. doi:10.1038/s41467-020-15074-6.

Tanay, A., Regev, A. Scaling single-cell genomics from phenomenology to mechanism. 2018.

Nature. 541(7637):331–338. doi:10.1038/nature21350

Uragami, C., D. Galzerano, A. Gall, Y. Shigematsu, M. Meisterhans, N. Oka, M. Iha, R. Fujii, B. Robert, and H. Hashimoto. 2014. Light-dependent conformational change of neoxanthin in a siphonous green alga, *Codium intricatum*, revealed by Raman spectroscopy. *Photosynth. Res.* 121:69–77. doi:10.1007/s11120-014-0011-y.

Walther, T.C., J. Chung, and R. V. Farese. 2017. Lipid droplet biogenesis. *Annu. Rev. Cell Dev. Biol.* 33:491–510. doi:10.1146/annurev-cellbio-100616-060608.

Wang, T., Y. Ji, Y. Wang, J. Jia, J. Li, S. Huang, D. Han, Q. Hu, W.E. Huang, and J. Xu. 2014. Quantitative dynamics of triacylglycerol accumulation in microalgae populations at single-cell resolution revealed by Raman microspectroscopy. *Biotechnol. Biofuels*. 7:1–12. doi:10.1186/1754-6834-7-58.

Wei, X., D. Jie, J.J. Cuello, D.J. Johnson, Z. Qiu, and Y. He. 2014. Trends in Analytical Chemistry Microalgal detection by Raman microspectroscopy. *Trends Anal. Chem.* 53:33–40. doi:10.1016/j.trac.2013.09.012.

Wiercigroch, E., E. Szafraniec, K. Czamara, M.Z. Pacia, K. Majzner, and K. Kochan. 2017. SC. *Spectrochim. Acta Part A Mol. Biomol. Spectrosc.* doi:10.1016/j.saa.2017.05.045.

Wood, B.R., P. Heraud, S. Stojkovic, D. Morrison, J. Beardall, and D. McNaughton. 2005. A portable Raman acoustic levitation spectroscopic system for the identification and environmental monitoring of algal cells. *Anal. Chem.* 77:4955–4961. doi:10.1021/ac050281z.

Wu, H., J. V. Volponi, A.E. Oliver, A.N. Parikh, B.A. Simmons, and S. Singh. 2011. In vivo lipidomics using single-cell Raman spectroscopy. *Proc. Natl. Acad. Sci.* 108:3809–3814. doi:10.1073/pnas.1009043108.

Yan, H., P. Zhang, C. Wang, Z. Liu, and W. Chang. 2007. Two lutein molecules in LHCII have different conformations and functions: Insights into the molecular mechanism of thermal dissipation in plants. *Biochem. Biophys. Res. Commun.* 355:457–463. doi:10.1016/j.bbrc.2007.01.172.

Zajac, G., J. Lasota, M. Dudek, A. Kaczor, and M. Baranska. 2017. Pre-resonance enhancement of exceptional intensity in Aggregation-Induced Raman Optical Activity (AIROA) spectra of lutein derivatives. *Spectrochim. Acta Part A Mol. Biomol. Spectrosc.* 173:356–360. doi:https://doi.org/10.1016/j.saa.2016.09.030.